



## 저작자표시-비영리-변경금지 2.0 대한민국

이용자는 아래의 조건을 따르는 경우에 한하여 자유롭게

- 이 저작물을 복제, 배포, 전송, 전시, 공연 및 방송할 수 있습니다.

다음과 같은 조건을 따라야 합니다:



저작자표시. 귀하는 원저작자를 표시하여야 합니다.



비영리. 귀하는 이 저작물을 영리 목적으로 이용할 수 없습니다.



변경금지. 귀하는 이 저작물을 개작, 변형 또는 가공할 수 없습니다.

- 귀하는, 이 저작물의 재이용이나 배포의 경우, 이 저작물에 적용된 이용허락조건을 명확하게 나타내어야 합니다.
- 저작권자로부터 별도의 허가를 받으면 이러한 조건들은 적용되지 않습니다.

저작권법에 따른 이용자의 권리는 위의 내용에 의하여 영향을 받지 않습니다.

이것은 [이용허락규약\(Legal Code\)](#)을 이해하기 쉽게 요약한 것입니다.

[Disclaimer](#)

Master's Thesis

석사 학위논문

Fabrication and characterization of thickness mode  
piezoelectric micromachined ultrasonic transducer  
(Tm-pMUT) based on PMN-PZT

Woojin Kang (강 우 진 姜 禍 珍)

Department of  
Robotics Engineering

**DGIST**

**2016**

Fabrication and characterization of thickness mode piezoelectric  
micromachined ultrasonic transducer (Tm-pMUT) based on PMN-PZT

Advisor : Professor Hongsoo Choi

Co-advisor : Professor Jae Youn Hwang

By

Woojin Kang

Department of Robotics Engineering

DGIST

A thesis submitted to the faculty of DGIST in partial fulfillment of the requirements for the degree of Master of Science in the Department of Robotics Engineering. The study was conducted in accordance with Code of Research Ethics<sup>1</sup>

01. 08. 2016

Approved by

Professor Hongsoo Choi  
(Advisor)

(Signature)

Professor Jae Youn Hwang  
(Co-Advisor)

(Signature)

---

<sup>1</sup> Declaration of Ethical Conduct in Research: I, as a graduate student of DGIST, hereby declare that I have not committed any acts that may damage the credibility of my research. These include, but are not limited to: falsification, thesis written by someone else, distortion of research findings or plagiarism. I affirm that my thesis contains honest conclusions based on my own careful research under the guidance of my thesis advisor.


Fabrication and characterization of thickness  
mode piezoelectric micromachined ultrasonic  
transducer (Tm-pMUT) based on PMN-PZT

Woojin Kang

Accepted in partial fulfillment of the requirements for the degree  
of Master of Science.

11. 13. 2015

Head of Committee     Prof. Hongsoo Choi



Committee Member     Prof. Jae Youn Hwang



Committee Member     Dr. Jungho Ryu



MS/RT  
201423001

강 우 진. Fabrication and characterization of thickness mode piezoelectric micromachined ultrasonic transducer (Tm-pMUT) based on PMN-PZT. Department of Robotics Engineering. 2016. 76p. Advisors Prof. Choi, Hongsoo, Co-Advisors Prof. Hwang, Jae Youn.

## ABSTRACT

In this study, the lead magnesium niobate–lead zirconate titanate (PMN-PZT) single crystal based thickness mode piezoelectric micromachined ultrasonic transducer (Tm-pMUT) array was fabricated using microelectromechanical systems (MEMS) process. The PMN-PZT single crystal was grown by solid-state single crystal growth (SSCG) method. The inductively coupled plasma (ICP) etching was used to make a PMN-PZT based Tm-pMUT array. The ICP etching characteristics of PMN-PZT single crystal were investigated in a  $\text{BCl}_3/\text{Cl}_2/\text{Ar}$  gas mixture environment. The ICP etching parameters were RF power, chamber pressure, bias power, gas mixing ratio. The RF power was varied from 200 W to 1000 W. The bias power was controlled from 50 W to 450 W, and the gas flow rate was fixed as 20 sccm. The PMN-PZT surface was analyzed using X-ray photoelectron spectroscopy (XPS) to investigate the etching mechanism. The result showed that the  $\text{BCl}_3/\text{Cl}_2/\text{Ar}$  plasma increased etch selectivity ratio without decreasing etch rate of PMN-PZT single crystal and the physical etching was dominant. The sidewall angles was increased along the increase of the bias power. The optimized ICP etching conditions were  $\text{BCl}_3/\text{Cl}_2/\text{Ar} = 5/2/3$  (10/4/6 sccm), 800 W RF power, 350 W bias power, 2 mTorr chamber pressure. The optimized ICP etching conditions gave a 107.6 nm/min etch rate and 4.22 etch selectivity ratio. Those optimized ICP conditions were used to fabricate the PMN-PZT based Tm-pMUT array. The PMN-PZT based Tm-pMUT array has 8 annular elements. The thickness of PMN-PZT single crystal was 300  $\mu\text{m}$ . The average resonance frequency and anti-resonance frequency were 2.66 ( $\pm 0.04$ ) and 3.18 ( $\pm 0.03$ ) MHz, respectively. The measured effective electromechanical coupling coefficient ( $k_{\text{eff}}^2$ ) was 30.05 %. These resonance frequency has high potential for ultrasound imaging applications.

**Keywords:** Piezoelectric, MEMS, PMN-PZT, Ultrasound, Piezoelectric micromachined ultrasonic transducer (pMUT)

# Contents

ABSTRACT .....	i
List of contents .....	ii
List of figures .....	iii
List of tables .....	iv
1. Introduction .....	8
1.1 Background knowledge .....	10
1.1.1 Dielectric material .....	10
1.1.2 Piezoelectric materials .....	12
1.2 Comparison between the material properties of the two piezoelectric materials; single crystals and PZT ceramics.....	19
1.3 Necessity of PMN-PZT ICP etching.....	20
1.4 Annular array transducer .....	22
1.5 The equivalent circuit of a piezoelectric vibrator .....	23
1.6 Related research work .....	25
1.6.1 Bulk piezoelectric transducer .....	25
1.6.2 Membrane type piezoelectric micromachined ultrasonic transducer (pMUT) .....	26
2. Design and Fabrications of PMN-PZT based Tm-pMUT array.....	27
2.1 Fabrication of the PMN-PZT single crystal.....	27
2.1.1 Grown PMN-PZT single crystal by using SSCG method.....	27
2.1.2 Hysteresis loop of PMN-PZT single crystal .....	29
2.2 Design of the PMN-PZT based Tm-pMUT array .....	31
2.3 Optimization of inductively coupled plasma (ICP) etching conditions for PMN-PZT based Tm-pMUT array.....	33
2.4 Fabrication Process of the PMN-PZT based Tm-pMUT array .....	36
3. Experiment .....	41
3.1 Impedance analysis of the PMN-PZT based Tm-pMUT array .....	41
4. Results and Discussions.....	43

4.1 PMN-PZT ICP etching results .....	43
4.1.1 The etch rate and etch selectivity ratio results of PMN-PZT/Ni.....	43
4.1.2 Effect of bias power on the sidewall angle of PMN-PZT single crystal .....	53
4.1.3 The X-ray photoelectron spectroscopy (XPS) analysis results of PMN-PZT single crystal .....	54
4.1.4 Discussion of PMN-PZT ICP etching.....	61
4.2 Electrical characterization of the PMN-PZT based Tm-pMUT array.....	62
4.2.1 Impedance analyzing of the kerfed type PMN-PZT based Tm-pMUT array .....	62
4.2.2 Impedance analyzing of the kerfless type PMN-PZT based Tm-pMUT array .....	65
4.2.3 Discussion on electrical characteristics of PMN-PZT based Tm-pMUT array .....	68
5. Conclusions .....	69
REFERENCES .....	71



## List of Figures

Figure 1.1 Categorization of dielectric materials.....	10
Figure 1.2 Schematic illustration of randomly generating charges in a dielectric material.....	11
Figure 1.3 Historic development of piezoelectric materials.....	13
Figure 1.4 Schematic graph of Paraelectric to Ferroelectric transition.....	15
Figure 1.5 Schematic graph of the relationship between hysteresis geometry and complex amplitudes of polarization.....	16
Figure 1.6 Schematic of the poling process in ferroelectric material, (a) before poling, (b) after poling.....	17
Figure 1.7 Hysteresis loop of the ferroelectric ceramic.....	18
Figure 1.8 The PMN-PT/epoxy 1-3 composite by using dicing saw.....	20
Figure 1.9 Schematic illustration of the ICP-RIE system.....	21
Figure 1.10 The axes of linear array.....	22
Figure 1.11 Equivalent circuit that is modeling for piezoelectric vibrator.....	23
Figure 1.12 Schematic of general bulk ceramic transducer. ....	25
Figure 1.13 Schematic illustration of membrane type pMUT. ....	26
Figure 2.1 Optical image of grown PMN-PZT single crystal.....	28
Figure 2.2 Schematic of corona poling process.....	30
Figure 2.3 Measured polarization of PMN-PZT single crystal.....	30
Figure 2.4 Schematic diagram of the PMN-PZT based Tm-pMUT array.....	32
Figure 2.5 Schematic procedure of PMN-PZT ICP etching. (a) SiO <sub>2</sub> was deposited by thermal wet oxidation, (b) silver paste was deposited for PMN-PZT adhesion, (c) Cr/Au was sputtered for seed layer, (e) SU-8 was patterned by photolithography for Ni patterning, (d) Ni was electroplated for hard mask, (e) SU-8 removal for lift-off, (f) Au/Cr/PMN-PZT dry etching by using Metal ICP-RIE system.....	35
Figure 2.6 Fabrication process of the PMN-PZT based Tm-pMUT array: (a) SiO <sub>2</sub> was deposited by thermal wet oxidation, (b) Ti/Pt was sputtered for bottom electrode, (c) silver paste was deposited for PMN-PZT adhesion, (d) Cr/Au was sputtered for seed layer, (e) SU-8 was patterned by photolithography for Ni patterning, (f) Ni was electroplated for hard mask, (g) SU-8 removal for lift-off, (h) Au/Cr/PMN-PZT was etched by Metal ICP-RIE system, (i) SU-8 was patterned by photolithography for top electrode patterning, (j) Ti/Pt was sputtered for top	

electrode, (k) SU-8 removal for lift-off, (l) Nonconductive epoxy was deposited for making a supporting layer, (m) Nonconductive epoxy was thermally cured.....	38
Figure 2.7 Optical images of PMN-PZT based Tm-pMUT array after (a) SU-8 patterned (b) Ni electroplated (c) ICP etched.....	39
Figure 2.8 Fabricated PMN-PZT based Tm-pMUT array (a) kerfed type PMN-PZT based Tm-pMUT array (b) kerfless type PMN-PZT based Tm-pMUT array.....	40
Figure 3.1 Optical image of ferroelectric test system.....	41
Figure 3.2 Optical image of impedance analyzer and probe station.....	42
Figure 4.1 Etch rate and etch selectivity ratio of PMN-PZT as a function of $\text{Cl}_2/\text{Ar}$ gas mixing ratio.....	44
Figure 4.2 Etch rate and etch selectivity ratio of PMN-PZT as a function of $\text{BCl}_3/\text{Ar}$ gas mixing ratio.....	45
Figure 4.3 Etch rate and etch selectivity ratio of PMN-PZT as a function of $\text{BCl}_3/\text{Cl}_2/\text{Ar}$ gas mixing ratio.....	47
Figure 4.4 Etch rate and etch selectivity ratio of PMN-PZT as a function of RF power.....	48
Figure 4.5 Etch rate and etch selectivity ratio of PMN-PZT as a function of Bias power.....	50
Figure 4.6 Comparative PMN-PZT etching results for RF power, Bias power and combination of optimized parameters.....	49
Figure 4.7 SEM micrographs of etched PMN-PZT single crystal at (a) 250 W bias power, (b) 350 W bias power and (c) 450 W bias power.....	53
Figure 4.8 XPS spectra of Pb 4f as variations of $\text{BCl}_3/\text{Cl}_2/\text{Ar}$ gas mixing ratio.....	55
Figure 4.9 XPS spectra of Zr 3d as variations of $\text{BCl}_3/\text{Cl}_2/\text{Ar}$ gas mixing ratio.....	56
Figure 4.10 XPS spectra of Ti 2p and Nb 3s as variations of $\text{BCl}_3/\text{Cl}_2/\text{Ar}$ gas mixing ratio.....	58
Figure 4.11 XPS spectra of Mg 1s as variations of $\text{BCl}_3/\text{Cl}_2/\text{Ar}$ gas mixing ratio.....	59
Figure 4.12 Impedance and phase analyzing results of the kerfed type PMN-PZT based Tm-pMUT array.....	63
Figure 4.13 Impedance and phase analyzing results of the kerfless type PMN-PZT based Tm-pMUT array.....	66

## List of Tables

Table 1.1 Material properties of PMN-PZT single crystal and PZT ceramics.....	19
Table 2.1 Design parameters of the PMN-PZT based Tm-pMUT array.....	31
Table 2.2 PMN-PZT ICP etching process parameters.....	34
Table 4.1 Etch rate and etch selectivity ratio of PMN-PZT/Ni as a function of Cl <sub>2</sub> /Ar gas mixing ratio.....	44
Table 4.2 Etch rate and etch selectivity ratio of PMN-PZT as a function of BCl <sub>3</sub> /Ar gas mixing ratio.....	46
Table 4.3 Etch rate and etch selectivity ratio of PMN-PZT as a function of BCl <sub>3</sub> /Cl <sub>2</sub> /Ar gas mixing ratio.....	47
Table 4.4 Etch rate and etch selectivity ratio of PMN-PZT as a function of Cl <sub>2</sub> /Ar gas mixing ratio.....	49
Table 4.5 Etch rate and etch selectivity ratio of PMN-PZT as a function of Bias power.....	50
Table 4.6 Comparative PMN-PZT etching results for RF power, Bias power and combination of optimized parameters.....	52
Table 4.7 Electric characterization of the kerfed type PMN-PZT based Tm-pMUT array.....	64
Table 4.8 Electric characterization of the kerfless type PMN-PZT based Tm-pMUT array.....	67

# 1. Introduction

The frequency range of ultrasound is above 20 kHz and ultrasound is a physical pressure. Since ultrasound is a kind of acoustic sound wave, ultrasonic imaging is the safest medical imaging system among the medical imaging systems such as computed tomography (CT), X-ray, magnetic resonance imaging (MRI), position emission tomography (PET), and etc.

Ultrasonic transducers are devices which transform electrical input energy into mechanical output energy or vice versa. Ultrasonic transducers are divided into two types by their fabrication method [1]. One is bulk ceramic transducer and the other one is micromachined ultrasonic transducer (MUT) using micro electro mechanical system (MEMS) technologies. Traditionally a bulk ceramic transducers have been fabricated by dicing and lapping bulk ceramics to yield devices that resonate in the through-thickness direction (33) [2]. Because of diamond dicing blade dimension, making the gaps between elements smaller than 50  $\mu\text{m}$  is difficult [3, 4]. Above all, the system made with ceramic based transducers is generally bulky [5]. Micromachined ultrasonic transducer (MUT) is being developed as an alternative to transducer fabricated from bulk ceramic transducer, as they offer the potential for direct integration of electrical connections, fine scale structuring [6, 7]. There are two kinds of MUTs by its operating principles. One is capacitive MUT (cMUT) [8, 9] and the other one is piezoelectric MUT (pMUT) [10, 11]. Although cMUT shows high bandwidth, however the acoustic power is generally smaller than pMUT because the displacement of the top electrode is limited to avoid pull-in effect [12]. Also, cMUT required high DC bias voltage for effective operation. However, pMUT does not need high DC bias voltage because it is operated by piezoelectric effect.

The operational frequency of these pMUT is dictated by their resonance frequency which is dictated by the thickness of the piezoelectric material [13]. For devices operating in the region of 1–10 MHz, this necessitates a thickness of hundreds of  $\mu\text{m}$ . Such thicknesses of piezoelectric ceramic can readily be achieved using bulk ceramic processing but are very difficult to obtain using film forming techniques typically employed for fabrication of pMUTs [13, 14]. For the advantages of pMUTs to be utilized in this frequency range, diaphragm type resonators can be constructed where the resonance is excited using a bending mode (31). By creating a diaphragm structure, a bending mode is induced where the resonance frequency is dictated by the diameter and thickness of the diaphragm [13].

The drive to enhance the acoustic power of ultrasonic transducer requires the use of higher piezoelectric charge constant [15]. In order to gain the high acoustic power, much larger diaphragms size are needed. As the dimension of the diaphragms increase, the ratio of active area relative to passive area (e.g., connections, dead space) decreases. Therefore thickness mode MUT suitable for high acoustic power applications without these problems.

This research presents the dry etching performances of PMN-PZT single crystal and Tm-pMUT array fabrication techniques.

## 1.1 Background knowledge

### 1.1.1 Dielectric material

Dielectric materials are an electric insulator that can be polarized by an external electric field. Dielectric material is the top concept of the other materials such as piezoelectric material, pyroelectric material and ferroelectric material (Figure 1.1).

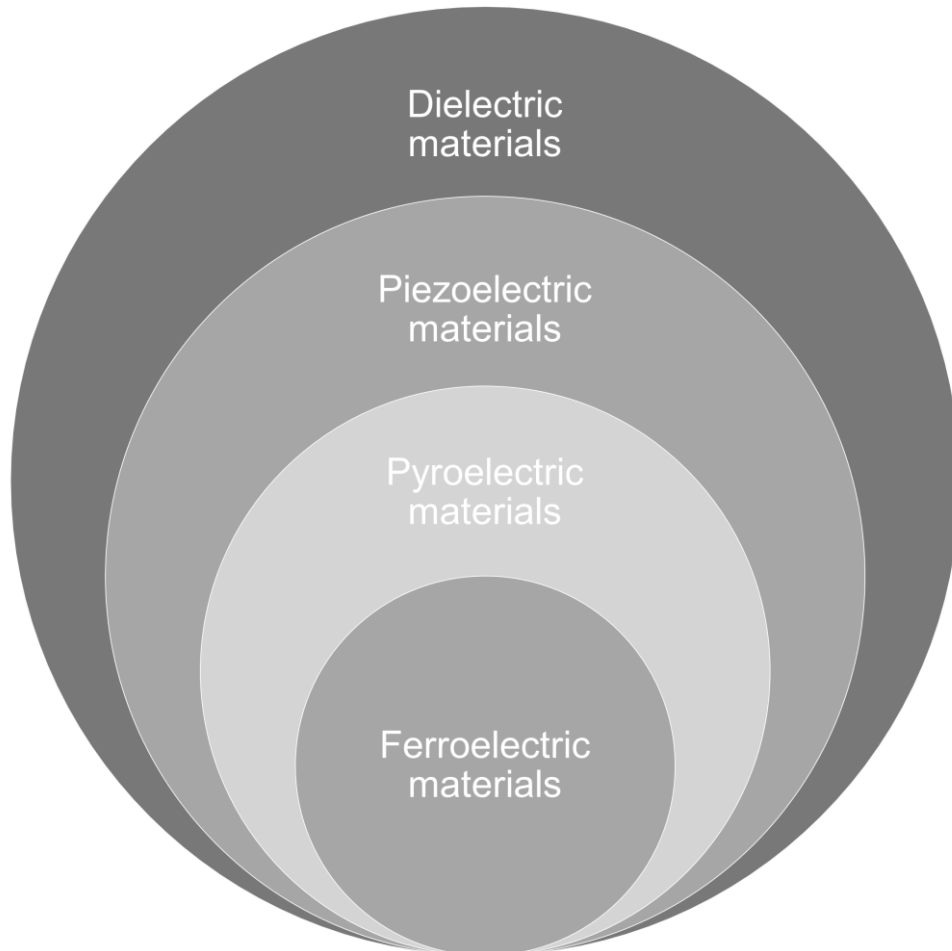


**Figure 1.1** Categorization of dielectric materials.

Dielectric materials can be described with regard to electrical characteristics such as permittivity, dielectric loss. In terms of transducers, the dielectrics can be characterized as field vectors and equivalent circuits [16]. On the other hand, the chemist have described of dielectrics with regard to molecular distortion and relaxation [17]. The molecular dipoles in a dielectric material are randomly generating charges (Figure 1.2).

## Random interfaces in dielectrics

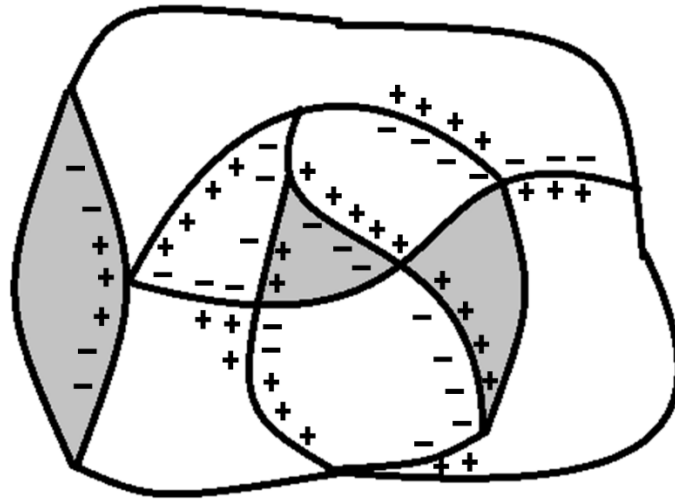


Figure 1.2 Schematic illustration of randomly generating charges in a dielectric material

To characterize dielectric properties of PMN-PZT single crystal, some fundamental characteristics were presented in this research such as hysteresis loop, piezoelectric behavior.

### **1.1.2 Piezoelectric materials**

#### **1.1.2.1 Historic development of piezoelectric materials**

The piezoelectric effect is the characteristic of piezoelectric materials. The piezoelectric material can convert electrical energy into mechanical energy or vice versa. The Pierre and Jacques Curie brother were the first to observe this phenomenon with topaz, cane sugar, quartz and tourmaline crystals in 1880 [18]. Barium Titanate ( $\text{BaTiO}_3$ ) was developed in 1948 [19]. It was the first practical ferroelectric based piezoelectric material. In 1952, Lead Zirconate Titanate ( $\text{Pb}(\text{Zr,Ti})\text{O}_3$ , PZT) was developed at the Tokyo institute of technology [20]. PZT is the most commonly used piezo ceramic today. Because PZT was physically strong, chemically stable, and inexpensive to fabricate ceramics. Lead Zinc Niobate-Lead Titanate ( $\text{Pb}(\text{Zr}_{1/3},\text{Nb}_{2/3})\text{O}_3\text{-PbTiO}_3$ , PZN-PT) and Lead Magnesium Niobate-Lead Titanate ( $\text{Pb}(\text{Mg}_{1/3},\text{Nb}_{2/3})\text{O}_3\text{-PbTiO}_3$ , PMN-PT) were developed by Jun Kuwata and Thomas R. Shrout [21, 22]. Those single crystals effects the piezoelectric research field. Because single crystal have higher piezoelectric constant than piezo ceramics generally (Figure 1.3) [23].



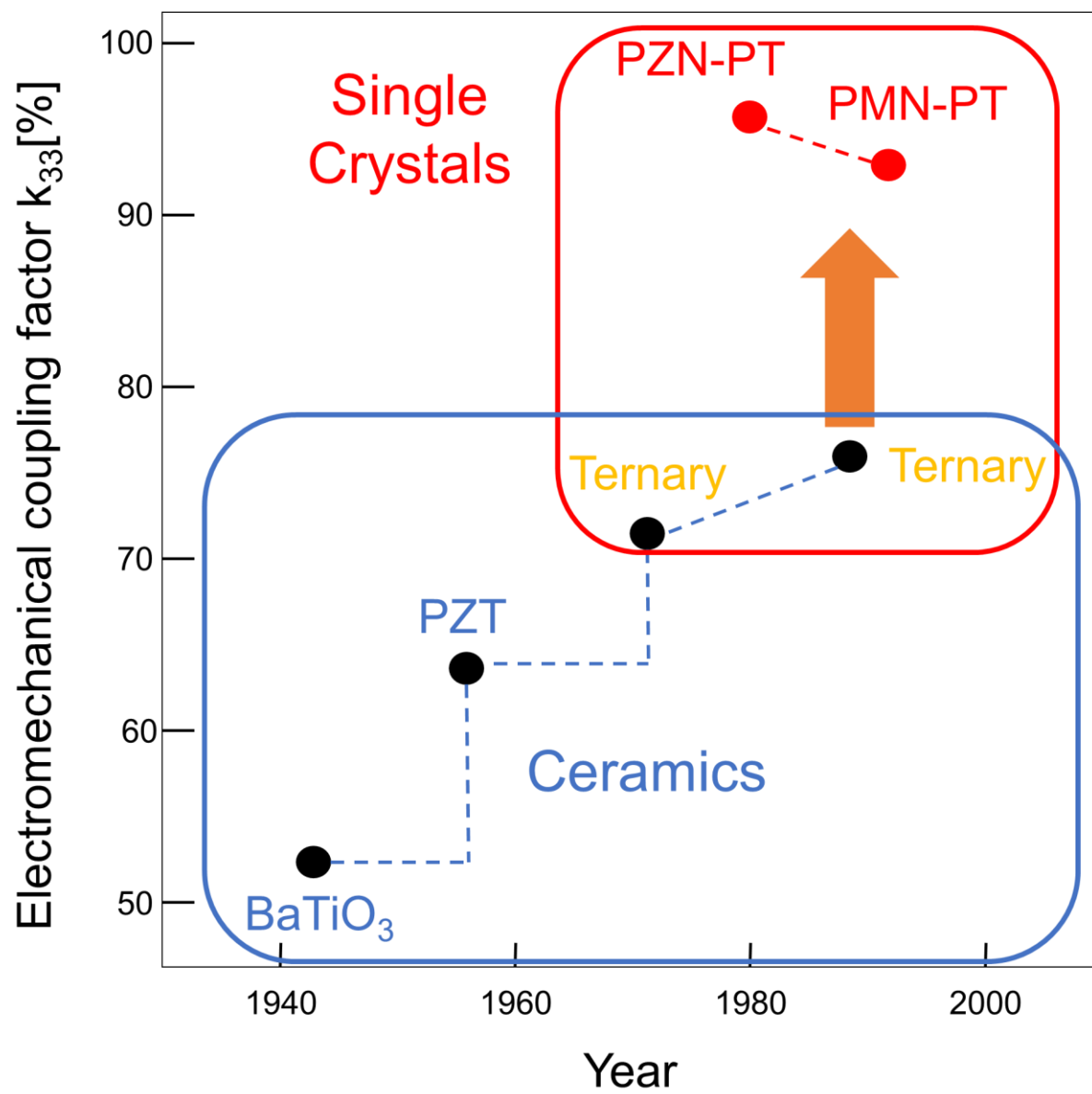


Figure 1.3 Historic development of piezoelectric materials.

### 1.1.2.2 Piezoelectricity

The word piezoelectricity is used to describe that the mechanical displacements are related to some degree to applied electric fields. When the electric field is applied, dipole is aligned to electric field direction. The piezoelectric material can change their shape by using applied external electric field and it is called as converse piezoelectric effect. On the other hand, when piezoelectric material is deformed, the piezoelectric material makes electric energy and it is called as direct piezoelectric effect.

The polarized piezoelectric materials can be characterized by Equation 1.1 and 1.2.

$$D = d \cdot T + \varepsilon^T \cdot E \quad (1.1)$$

$$S = s^E \cdot T + d \cdot E \quad (1.2)$$

Here,  $D$  is the dielectric displacement,  $d$  is the piezoelectric charge coefficient,  $T$  is the mechanical stress, this stress is localized on a plane along to the applied direction (Figure 1.2),  $\varepsilon^T$  is the permittivity at constant stress,  $E$  is the electric field,  $S$  is the mechanical strain,  $s^E$  is the compliance or elasticity coefficient [24].

.

### 1.1.2.3 Spontaneous and Remanent polarization

Ferroelectric material can be polarization. When external electric field is applied to ferroelectric material, the external electric field makes a reorientation of the dipoles and it is called spontaneous polarization. It means that even if the external electric field was eliminated, a little polarization is remained. The remained polarization is called remanent polarization.

For example, a PZT ceramic has a paraelectric phase and a cubic form at high temperature. However, below the Curie temperature, a PZT ceramic has ferroelectric phase of tetragonal, rhombohedral structure forms. It means that the spontaneous polarization is disappeared above Curie temperature (Figure 1.4).

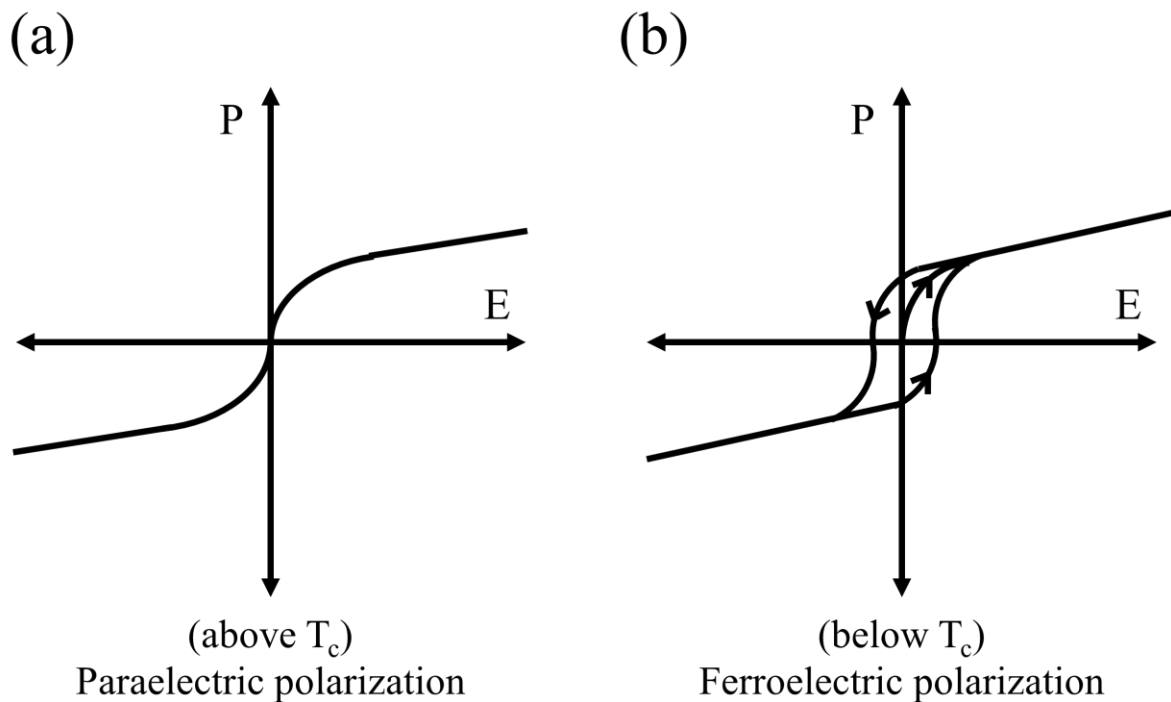


Figure 1.4 Schematic graph of Paraelectric to Ferroelectric transition.

#### 1.1.2.4 Hysteresis loop

The polarization of ferroelectric material is generally modeled via the Rayleigh Equation 1.3 [25].

$$P = (\chi + pE_0)E \mp \frac{p}{2}(E_0^2 - E^2) \quad (1.3)$$

This equation can be developed into Fourier series of the electric field (Figure 1.5) [26]. It describes the hysteresis loop relation between the polarization and an electric field applied to a ferroelectric material

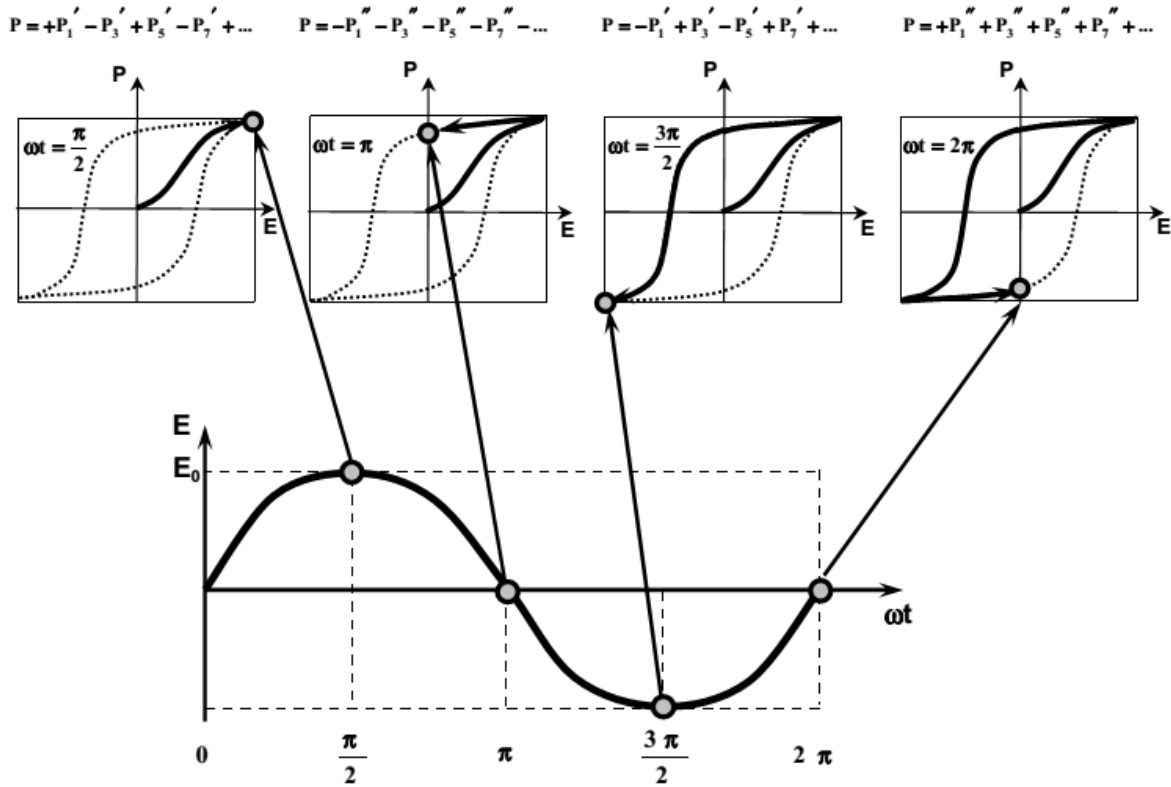


Figure 1.5 Schematic graph of the relationship between hysteresis geometry and complex amplitudes of polarization [26].

The ferroelectric polarization starts for an unpoled state and then increase of the polarization (Figure 1.7 between A and B). However, within this region, the dipole is not totally reoriented along the external field direction yet. Domains favorable to a reorientation need a stronger field to switch orientation (Figure 1.7 between B and C). Finally, all the dipoles are

switched, the polarization response becomes linear along with increase in electric field (Figure 1.7 between C and D). At this time, the maximum polarization is saturation polarization. When the external electric field is removed, a spontaneous polarization will be decreased (Figure 1.7 between D and E). At zero electric field, the remained polarization is remnent polarization. This process is called Poling process (Figure 1.6).

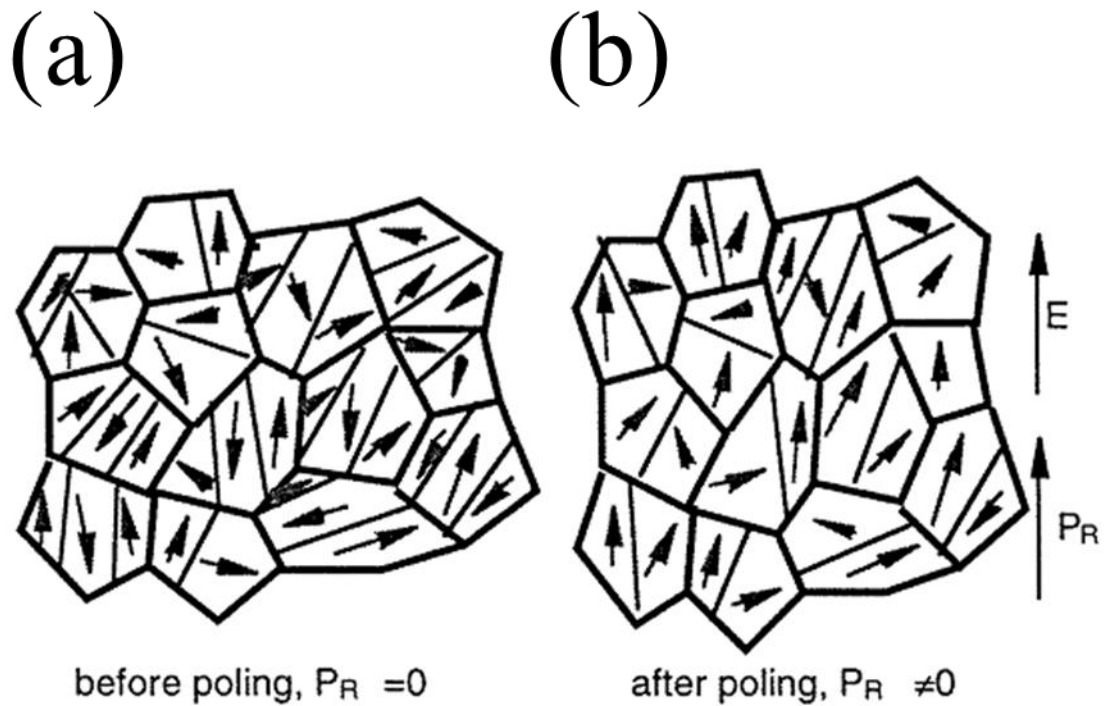


Figure 1.6 Schematic of the poling process in ferroelectric material, (a) before poling, (b) after poling [27].

To make the polarization value of the ferroelectric material returns to zero, the external electric field applied opposite direction (Figure 1.7 between E and F). The applied external electric field is called the coercive field. Continuously, when the external electric field is applied higher than coercive field, it makes the opposite maximum polarization (Figure 1.7 between F and G). When the external electric field is removed, an opposite spontaneous polarization will be decreased.

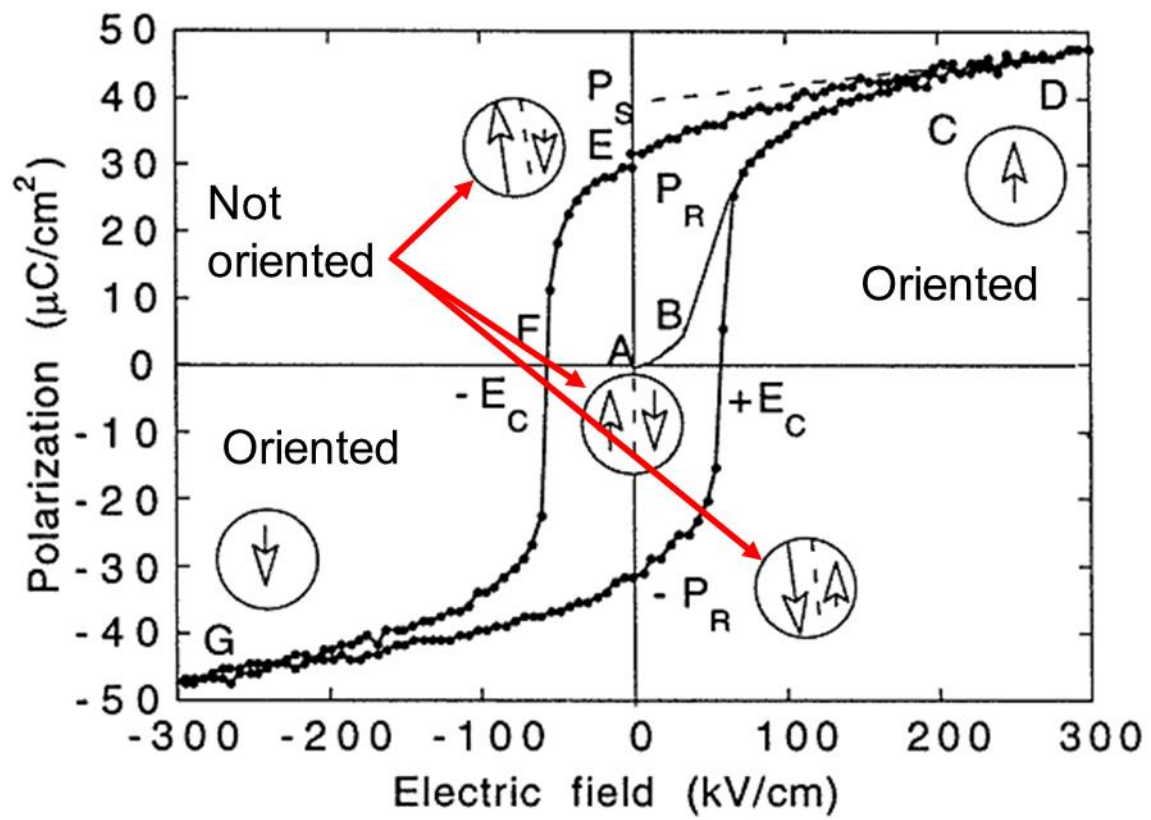


Figure 1.7 Hysteresis loop of the ferroelectric ceramic [27].

## 1.2 Comparison between the material properties of the two piezoelectric materials; single crystals and PZT ceramics

In general, PZT ceramics are widely chosen because they are physically strong, chemically inert, and inexpensive to fabricate [28]. However, compared to PZT ceramics, lead-based piezoelectric single crystals including PMN-PT, PZN-PT, PMN-PZT ( $\text{Pb}(\text{Mg}_{1/3}\text{Nb}_{2/3})\text{O}_3\text{-Pb}(\text{Zr,Ti})\text{O}_3$ ) has many advantages. These piezoelectric single crystals have high piezoelectric constant, dielectric constant, and electromechanical coupling factor. So, the piezoelectric single crystal has a potential for applications in novel sensors and actuators. However, the piezoelectric single crystal has some disadvantages such as low Curie temperature and brittle material characteristic. The patterning of piezoelectric single crystal is more difficult than that of PZT ceramic.

**Table 1.1 Material properties of PMN-PZT single crystal and PZT ceramics.**

Material	Dielectric constant (pC/N)	EM coupling factor $k_{33}$	Piezoelectric constant ( $d_{33}$ )	Curie temperature ( $^{\circ}\text{C}$ )
PZT-5A [29]	1700	0.7	374	310
PZT-5H [29]	3400	0.75	593	250
PZT-4 [29]	1300	0.7	296	310
PZT-8 [29]	1000	0.64	225	320
PMN-PZT (CPSC 160-95) [30]	7000	0.93	2,000	160

### 1.3 Necessity of PMN-PZT ICP etching

The PMN-PZT single crystal is researched in variable research area due to piezoelectric constant ( $d_{33}$ ) of 2000 pC/N and electromechanical coupling coefficient ( $k_{33}$ ) of 0.9 [30-35].

Previously, the dicing saw or lapping have been chosen in order to process a piezoelectric single crystal (Figure 1.8) [36, 37]. However, the minimum dimension of diamond blade in dicing saw equipment is 15 ~ 20  $\mu\text{m}$  [38]. Therefore, it requires special processing using a plasma to process fine patterns. [39]. However, the dry etching characteristics of PMN-PZT single crystal are not reported well. Thus, dry etching process was carried out studies using a plasma to form a structure having fine patterns with a vertical etching profile.

The figure 1.9 shows schematic illustration of the ICP-RIE system (FabStar+, TTL, Korea).

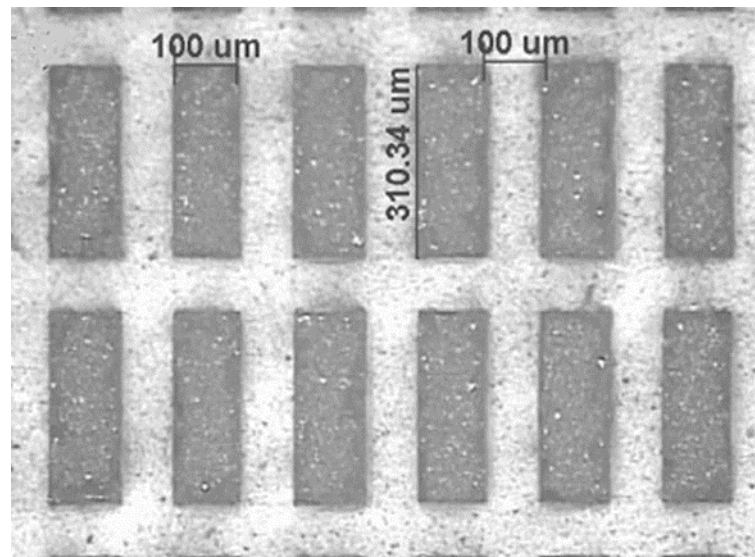


**Figure 1.8 The PMN-PT/epoxy 1-3 composite by using dicing saw [36].**



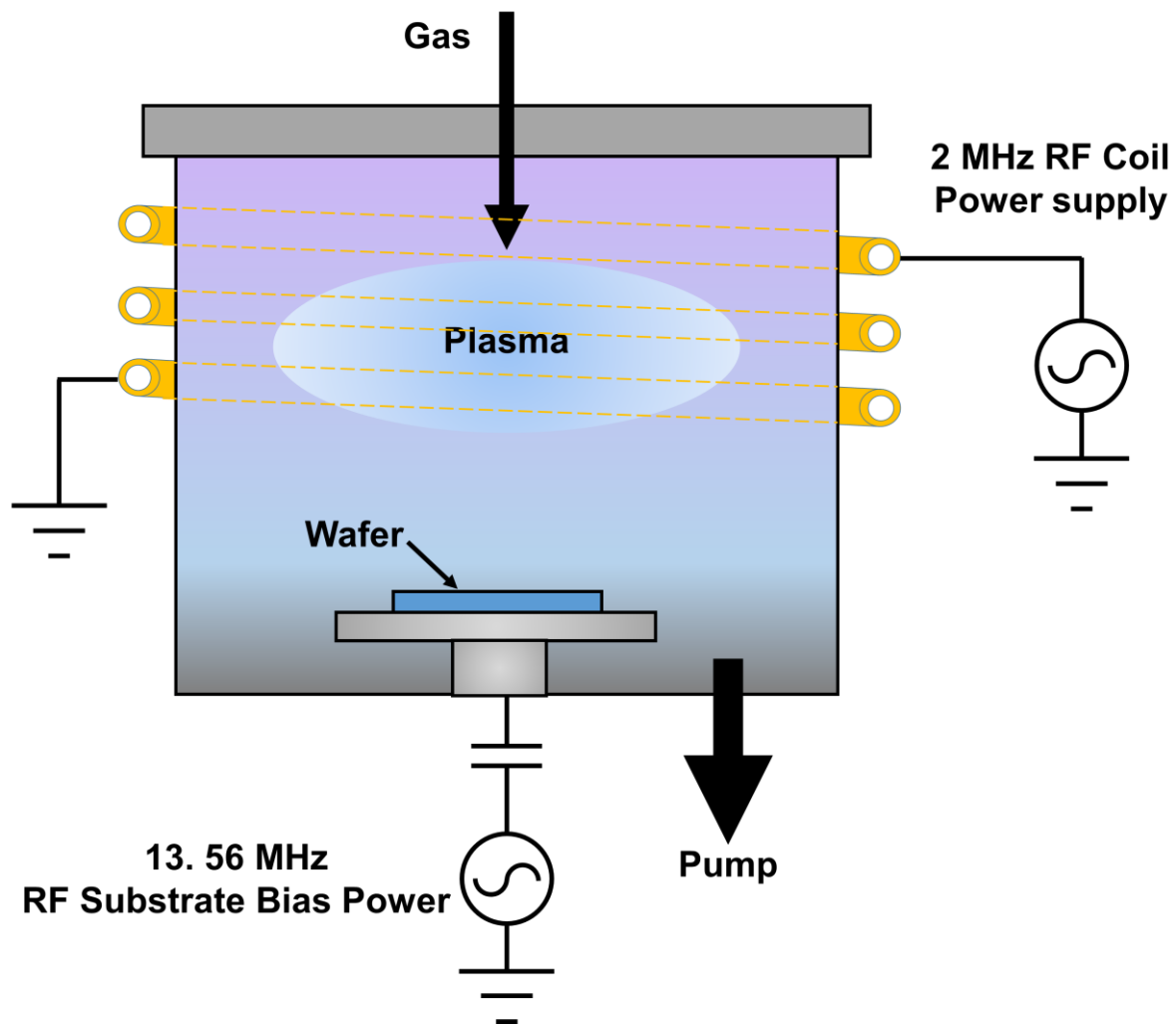


Figure 1.9 Schematic illustration of the ICP-RIE system.

## 1.4 Annular array transducer

The advantages of annular array shapes can be summarized as follows. First, an annular array has high uniform lateral resolution at far from the focal zone [40]. Thus an annular array can attain a large depth of field compared to a single element transducer. Second, the linear array transducer can dynamically focus only in the lateral direction and the lens determine only one focal point in the elevation direction (Figure 1.10) [41]. However, the annular array transducer can dynamic focus in both these lateral directions [42]. The PMN-PZT based Tm-pMUT array consists of a several concentric annuli. By using electrical delay, this arrangement can control focal depth along to the beam axis. The elements operated in order from the outside. Third, in the field of ultrasound imaging system, array based transducer require lots of elements for dynamic focusing and beam steering [43, 44]. However, annular array transducer can make imaging with less number of elements [45-47].

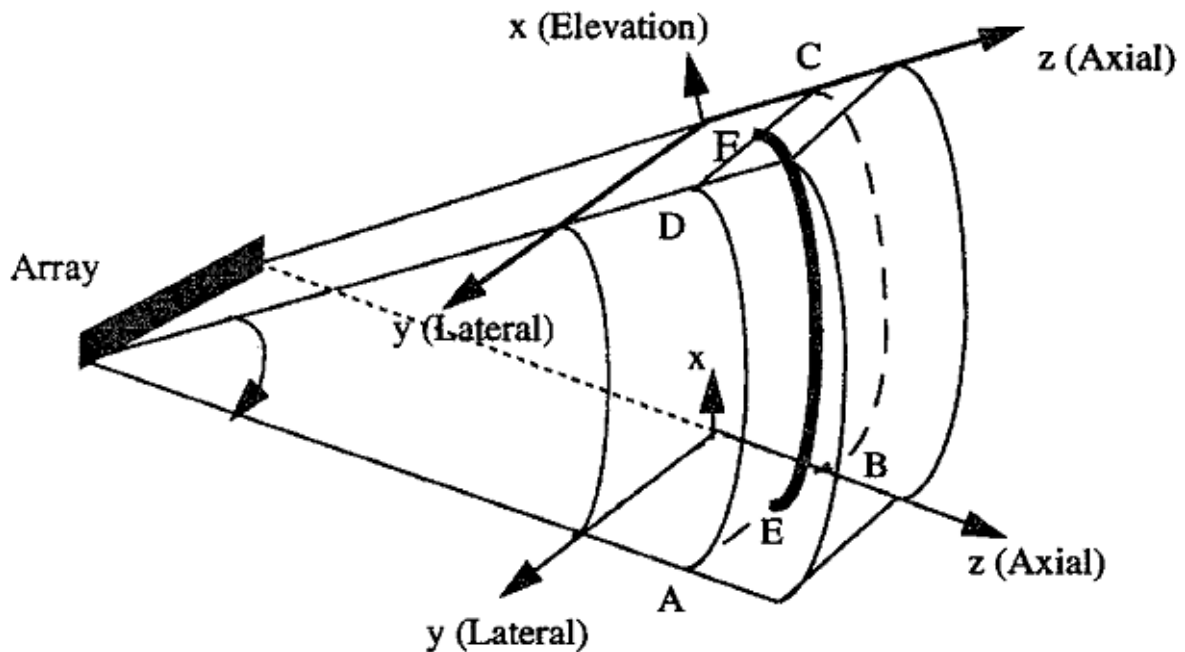


Figure 1.10 The axes of linear array [41].

## 1.5 The equivalent circuit of a piezoelectric vibrator

The figure 1.11 represented the equivalent circuit for piezoelectric vibrator. The electrical resonance frequency and anti-resonance frequency can be derived by Equation 1.4 and 1.5 [48].

$$f_r = \frac{1}{2\pi\sqrt{C_1 L_1}} \quad (1.4)$$

$$f_a = \frac{1}{2\pi} \sqrt{\frac{C_1 + C_0}{C_0 C_1 L_1}} \quad (1.5)$$

Where,  $L_1$ ,  $R_1$  and  $C_1$  represent the inductance, resistance and capacitance, respectively in series,  $C_0$  present parallel capacitance of the piezoelectric vibrator.

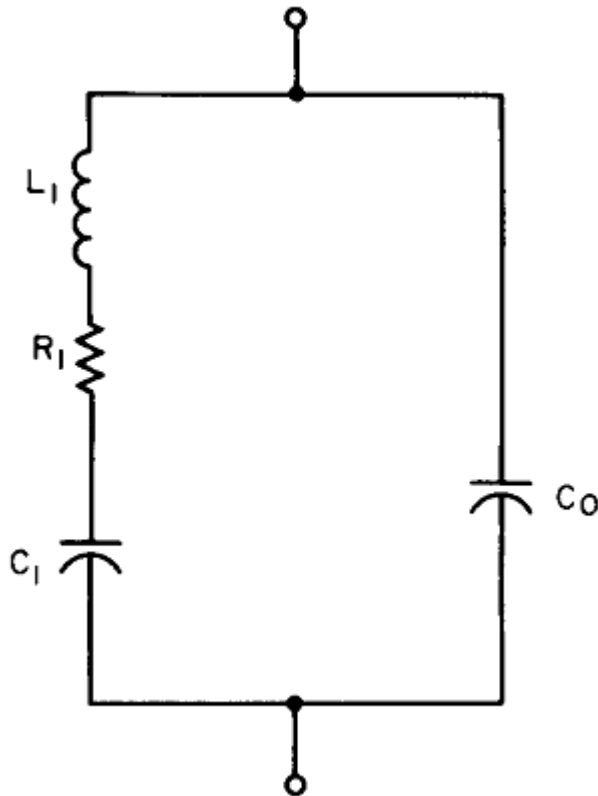


Figure 1.11 Equivalent circuit that is modeling for piezoelectric vibrator [24].

The effective electromechanical coupling factor ( $k_{eff}$ ) related with the resonance frequency and anti-resonance frequency. And effective electromechanical coupling factor can be calculated by Equation 1.6 [24].

$$k_{eff}^2 = \frac{C_1}{C_0 + C_1} = \frac{f_a^2 - f_r^2}{f_a^2} \quad (1.6)$$

The coupling coefficient is used to evaluate the performances of the piezoelectric transducer.

## 1.6 Related research work

### 1.6.1 Bulk piezoelectric transducer

Generally, bulk piezoelectric transducer was widely used for variable applications. Because bulk ceramic transducers have a high effective coupling coefficient. The bulk ceramic can generate high intensity ultrasound. The figure 1.12 shows a general bulk piezoelectric transducer. However, this transducer has some limitations. Generally the bulk ceramic transducers have been fabricated by dicing and lapping bulk piezoelectric materials to yield devices that resonate in the through-thickness direction (33) [2]. However, according to  $\lambda/2$  pitch rule for designing transducer array, for high frequency is hard to dice by traditional method. Therefore, general bulk piezoelectric transducer systems have large volume.

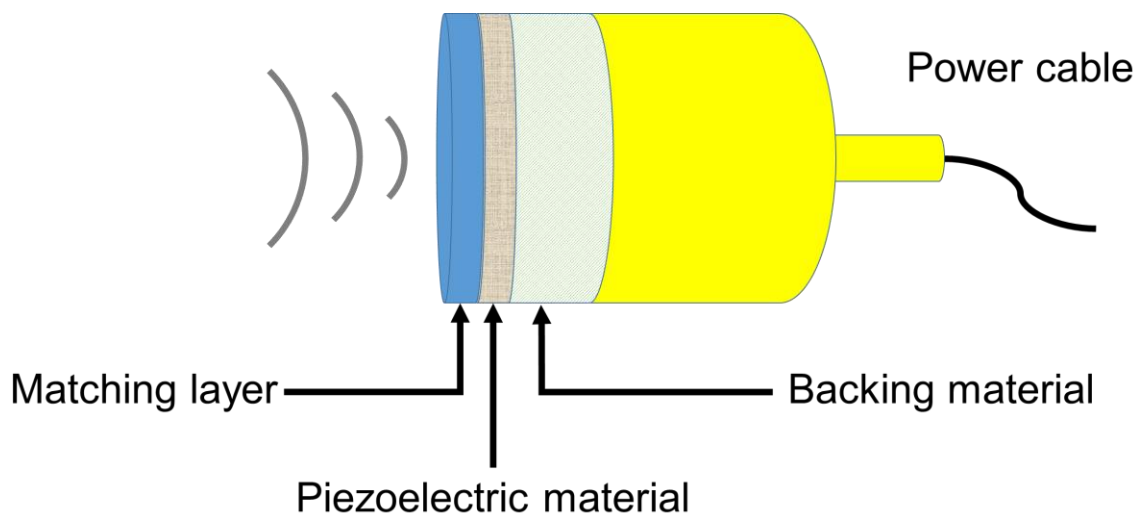


Figure 1.12 Schematic of general bulk piezoelectric transducer.

### 1.6.2 Membrane type piezoelectric micromachined ultrasonic transducer (pMUT)

To overcome the limitation of dicing process for a bulk piezoelectric transducer, the micro-electro-mechanical-system (MEMS) technologies are adopted. The figure 1.13 shows the schematic illustration of membrane type pMUT. The MEMS technology makes it possible to separate each element. The membrane type pMUT has some advantages over conventional bulk type ultrasonic transducer. Compared to bulk piezoelectric transducer, the space efficiency is high. Also, total system dimension is smaller than bulk transducer. Because of this advantages, pMUT has a potential to replace the bulk piezoelectric transducer in some research areas like cell stimulation, cell manipulation. However, membrane type pMUT also have some disadvantages. Their acoustic intensity is weaker than acoustic intensity of bulk transducer. The electromechanical coupling factor is much smaller than bulk transducer. To overcome this problem, this research propose the thickness-mode pMUT based PMN-PZT single crystal. The thickness-mode pMUT have bulk transducer's characteristics like high intensity, high electromechanical coupling factor.

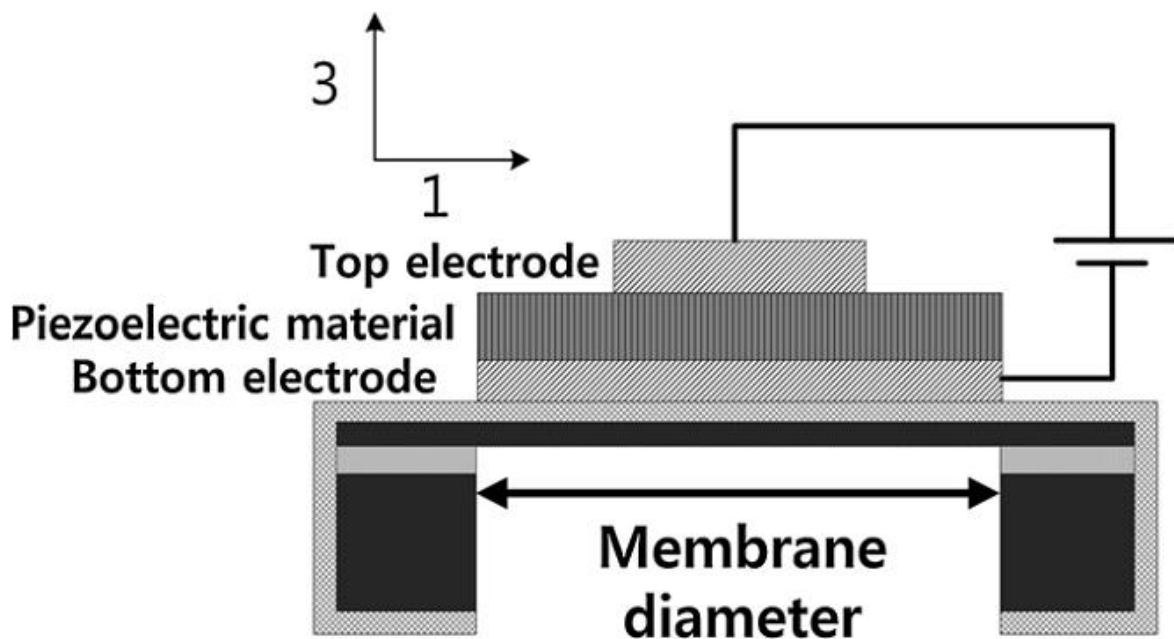


Figure 1.13 Schematic illustration of membrane type pMUT [49].

## **2. Design and Fabrications of PMN-PZT based Tm-pMUT array**

### **2.1 Fabrication of the PMN-PZT single crystal**

#### **2.1.1 Grown PMN-PZT single crystal by using SSCG method**

In this research, the PMN-PZT single crystal (CPSC 150-85, Ceracomp Co., Korea) was grown by solid-state single crystal growth (SSCG) method [50-53]. The 99.9 %  $\text{Pb}_3\text{O}_4$  (Alfa Aesar, Ward Hill, MA), the 99.9 %  $\text{MgNb}_2\text{O}_6$  (H. C. Starck GmbH, Newton, MA) and the 99.9 %  $\text{TiO}_2$  (Ishihara, San Francisco, CA) was used to fabricate PMN-PZT single crystal. Each raw powder materials was mixed by ball milling process for a 24 hours. then, the mixture was dried. After drying process, the mixture was calcinated in 800 °C. The mixture was mixed with  $\text{PbO}$  power by ball milling process again. After drying process, the mixture was molded by compression molding method. The mixture was sintered. After the mixture was sintered, the seed crystal was bonded to polycrystalline body. The polycrystalline body with seed crystal was heat treated to convert the ceramics to single crystals. The dimension of the grown PMN-PZT single crystal was 20 x 20 x 0.3 mm<sup>3</sup> (Figure 2.1).

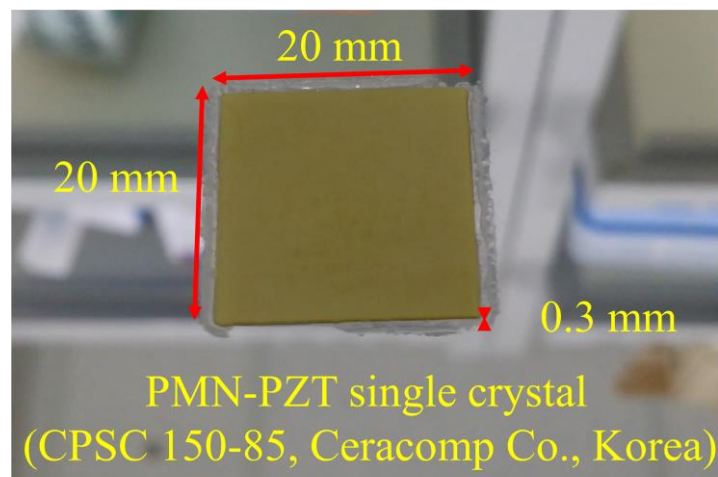


**Figure 2.1 Optical image of grown PMN-PZT single crystal.**



### **2.1.2 Hysteresis loop of PMN-PZT single crystal**

The corona poling was conducted to investigate the hysteresis of PMN-PZT single crystal. The applied electric field was 6 kV and processing time was 30 minutes. When corona discharge was a partial breakdown the air, and was initiated by discharge in an inhomogeneous electric field. The all of individual dipole moments of PMN-PZT single crystal were aligning. So, all dipole moments point in the same general direction (Figure 2.2).

The poled PMN-PZT single crystal was measured the polarization by ferroelectric test system (Precision LC II, Radiant Technologies, USA).

The measured polarization showed that the PMN-PZT single crystal had soft piezoelectric material's behavior (Figure 2.3). Because the coercive field range was quite small. So, the PMN-PZT single crystal is candidate for applications in sensors and actuators.

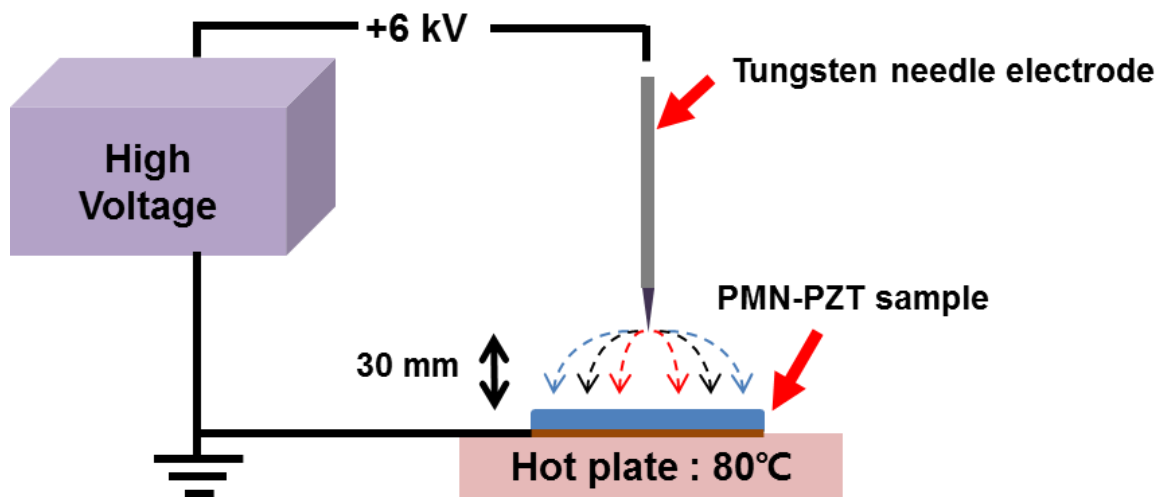


Figure 2.2 Schematic of corona poling process.

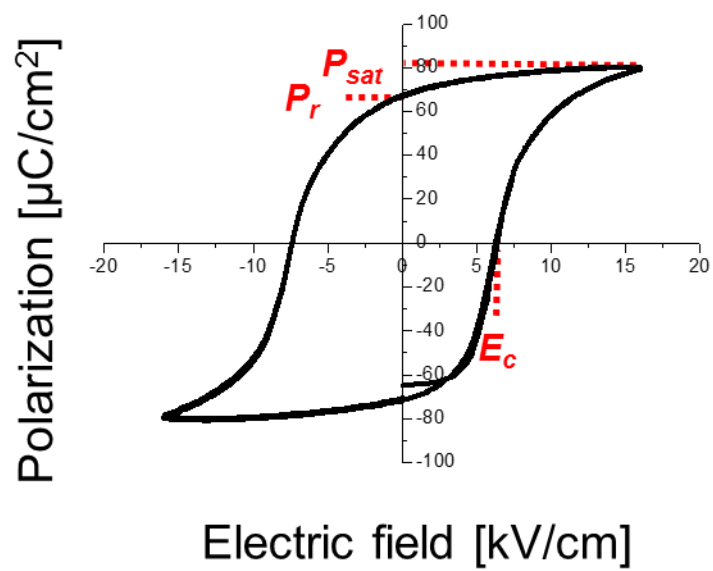


Figure 2.3 Measured polarization of PMN-PZT single crystal.

## 2.2 Design of the PMN-PZT based Tm-pMUT array

The table 2.1 showed design parameters of the PMN-PZT based Tm-pMUT array. The PMN-PZT based Tm-pMUT array had 8 elements. The thickness of the PMN-PZT was 300  $\mu\text{m}$ . It was designed annular array shape and each pMUT elements operated  $k_{33}$  mode (Figure 2.4).

**Table 2.1 Design parameters of the PMN-PZT based Tm-pMUT array.**

PMN-PZT based Tm-pMUT array				
Elements dimension	120 $\mu\text{m}$ (width)	920 $\mu\text{m}$ (dia.)	Area	0.0028 (cm <sup>2</sup> )
		1720 $\mu\text{m}$ (dia.)		0.0056 (cm <sup>2</sup> )
		2520 $\mu\text{m}$ (dia.)		0.0084 (cm <sup>2</sup> )
		3320 $\mu\text{m}$ (dia.)		0.0112 (cm <sup>2</sup> )
		4120 $\mu\text{m}$ (dia.)		0.0141 (cm <sup>2</sup> )
		4920 $\mu\text{m}$ (dia.)		0.0169 (cm <sup>2</sup> )
		5720 $\mu\text{m}$ (dia.)		0.0197 (cm <sup>2</sup> )
		6520 $\mu\text{m}$ (dia.)		0.0225 (cm <sup>2</sup> )
Num. of Elements	8			
Thickness	300 $\mu\text{m}$			

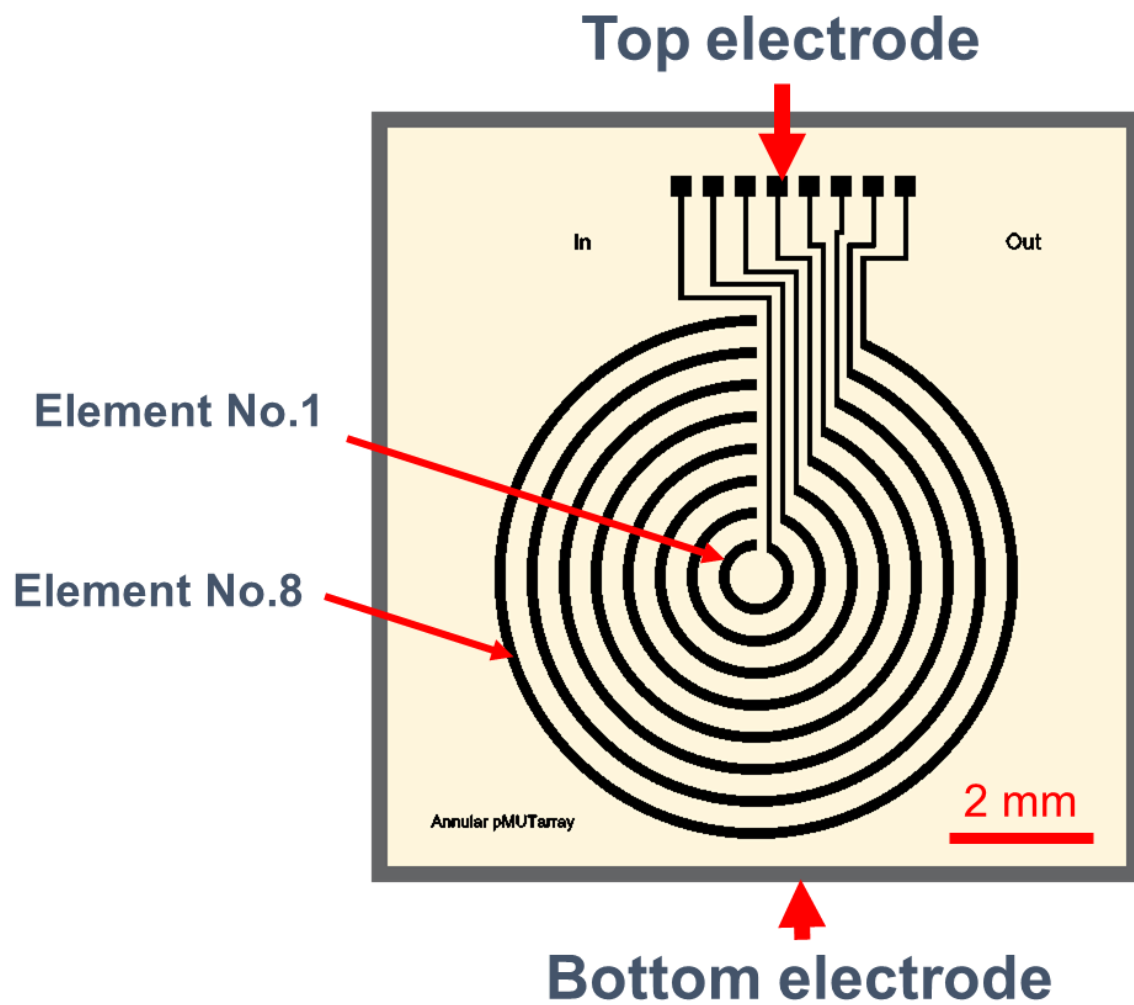


Figure 2.4 Schematic diagram of the PMN-PZT based Tm-pMUT array.

## **2.3 Optimization of inductively coupled plasma (ICP) etching conditions for PMN-PZT based Tm-pMUT array**

In this research, the dry etching characteristics of PMN-PZT single crystal was investigated using an inductively coupled plasma (ICP) etching system. The  $\text{BCl}_3/\text{Cl}_2/\text{Ar}$  gas mixture was used to make a plasma. The controlled process parameters were RF power, chamber pressure, bias power, gas mixing ratio. The RF power was varied from 200 W to 1000 W. The bias power was controlled from 50 W to 450 W, and the gas flow rate was fixed as 20 sccm. The etched PMN-PZT surface was analyzed by X-ray photoelectron spectroscopy (XPS) to investigate the etching mechanism.

The PMN-PZT single crystal (CPSC 150-85, Ceracomp Co., Korea) was grown by solid-state single crystal growth (SSCG) method [50-53]. Because this SSCG method can make the irregular structure of polycrystalline ceramic into precise piezoelectric single crystal without melting the components [54]. The dimension of the grown PMN-PZT single crystal was 20 x 20 x 0.3 mm<sup>3</sup>. The figure 2.5 shows schematic procedure of PMN-PZT ICP etching process.

First, 6 inch Si wafer was prepared. The  $\text{SiO}_2$  was deposited 1.13  $\mu\text{m}$  thick by thermally wet oxidation. The  $\text{SiO}_2$  layer was used to make insulator. To bond the PMN-PZT single crystal, the silver paste (ELCOAT, CANS, Japan) was deposited 5  $\mu\text{m}$  thick for high adhesion between PMN-PZT single crystal and wafer (Figure 2.5 (a)). After PMN-PZT bond, the Cr 200 nm/Au 200 nm was sputtered on the wafer which was used to make Ni seed layer (Figure 2.5 (b)). After the seed layer was sputtered, SU-8 (SU-8 2100, MicroChem, USA) was spin coated 58  $\mu\text{m}$  thick and patterned by the photolithography. The SU-8 was used to make a mold for Ni as a hard mask for ICP patterning (Figure 2.5 (c)). After the SU-8 was patterned, the Ni was deposited 10  $\mu\text{m}$  by electroplating (Figure 2.5 (d)). The SU-8 was removed by acetone and sonicator (Figure 2.5 (e)). After the Ni hard mask was formed, the Au/Cr/PMN-PZT was etched

using Metal ICP-RIE system (Figure 2.5 (f)). The working pressure was fixed at 2 mTorr for high uniformity.

The table 2.2 presented PMN-PZT ICP etching process parameters. The etching times was 300 sec per each process. The etch rate and etch selectivity ratio were investigated by surface profiler (Dektak XT, Bruker, USA). After the PMN-PZT single crystal was etched, the PMN-PZT single crystal was exposed to the atmosphere for about 24 hours for removing the volatile etch product. The PMN-PZT surface was investigated using XPS (ESCALAB 250Xi, Thermo scientific, U.K.) to analyze chemical reaction between PMN-PZT single crystal and radicals. The PMN-PZT surface was narrow scanned. The Pb, Mg, Nb, Zr and Ti were observed their change in the peak intensities and core binding energy shifts. X-ray source used in the XPS analysis, has an energy of 1486.6 eV as Al ( $K\alpha$ ).

**Table 2.2 PMN-PZT ICP etching process parameters.**

Run No.		a-1 ~ a-5	b-1 ~ b-5	c-1 ~ c-5	d-1 ~ d-5	e-1 ~ e-5	f
RF power	W	600			200 ~ 1000	600	800
Bias power	W	250			250	50 ~ 450	350
Gas flow rate (sccm)	Total	20					
	BCl <sub>3</sub>	0	0 ~ 20	0 ~ 14	10		10
	Cl <sub>2</sub>	0 ~ 20	0	14 ~ 0	4		4
	Ar	20 ~ 0	20 ~ 0	6	6		6
Working pressure	mT	2					
Etching time	min	5					
Mask		Ni					

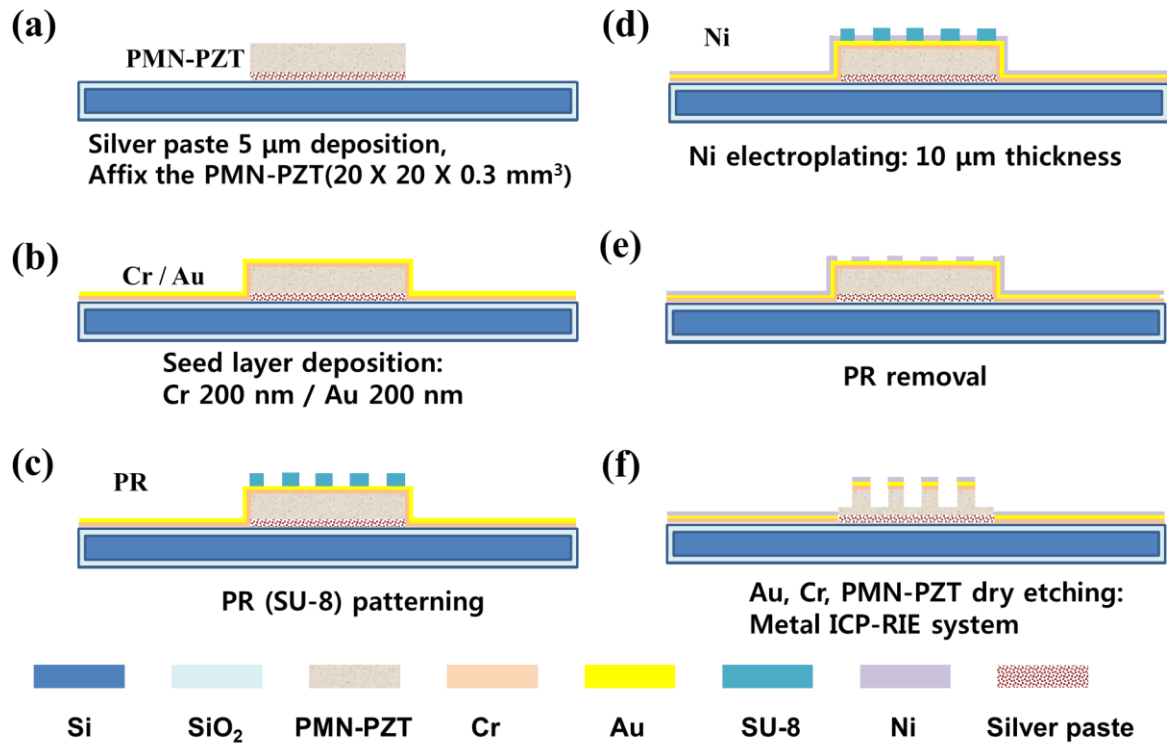


**Figure 2.5 Schematic procedure of PMN-PZT ICP etching.** (a)  $\text{SiO}_2$  was deposited by thermal wet oxidation, (b) silver paste was deposited for PMN-PZT adhesion, (c) Cr/Au was sputtered for seed layer, (e) SU-8 was patterned by photolithography for Ni patterning, (d) Ni was electroplated for hard mask, (e) SU-8 removal for lift-off, (f) Au/Cr/PMN-PZT dry etching by using Metal ICP-RIE system.

## 2.4 Fabrication Process of the PMN-PZT based Tm-pMUT array

The PMN-PZT based Tm-pMUT array was fabricated by MEMS process. The fabrication process was presented in figure 2.6. First, 6 inch Si wafer was prepared. The SiO<sub>2</sub> was deposited 1.13  $\mu\text{m}$  thick by thermally wet oxidation. The SiO<sub>2</sub> layer was used to make insulator (Figure 2.6 (a)). To make bottom electrode layer, the Ti 20 nm/Pt 180 nm was sputtered on the SiO<sub>2</sub> layer. The Ti was used to make adhesive layer (Figure 2.6 (b)). The silver paste (ELCOAT, CANS, Japan) was deposited 5  $\mu\text{m}$  thick for high adhesion between PMN-PZT single crystal and wafer. The PMN-PZT single crystal (CPSC 150-85, Ceracomp Co., Korea) was grown by SSCG method. The dimension of PMN-PZT single crystal was 20 x 20 x 0.3 mm<sup>3</sup> (Figure 2.6 (c)). After PMN-PZT bond, the Cr 200 nm/Au 200 nm was sputtered on the wafer which was used to make Ni seed layer (Figure 2.6 (d)). After the seed layer was sputtered, SU-8 (SU-8 2100, MicroChem, USA) was spin coated 58  $\mu\text{m}$  thick and patterned by the photolithography (Figure 2.6 (e)). The SU-8 was used to make a mold for Ni patterning (Figure 2.7 (a)). After the SU-8 was patterned, the Ni was deposited 20  $\mu\text{m}$  by electroplating (Figure 2.6 (f)). The Ni was used as hard mask for ICP patterning. The SU-8 was removed by acetone and sonicator (Figure 2.6 (g) and Figure 2.7 (b)). After the Ni hard mask was formed, the Au/Cr/PMN-PZT was etched using Metal ICP-RIE system to reduce cross talk (Figure 2.6 (h)) [55, 56]. The Au/Cr/PMN-PZT was dry etched using BCl<sub>3</sub>/Cl<sub>2</sub>/Ar= 5/3/2 (10/6/4 sccm), The other ICP conditions such as RF power, Bias power, working pressure were fixed at 800 W, 350 W, 2 mTorr, respectively. The etch rate of PMN-PZT single crystal was 107.6 nm/min and etch selectivity ratio with Ni was 4.22. The total etch depth of PMN-PZT single crystal was 30  $\mu\text{m}$  (Figure 2.7 (c)). After the PMN-PZT single crystal was etched, SU-8 was spin coated 58  $\mu\text{m}$  and patterned by the photolithography again. The SU-8 was patterned for making top electrode by lift-off process (Figure 2.6 (i)). To make top electrode layer, the Ti 20 nm/Pt



180 nm was sputtered on the wafer again (Figure 2.6 (j)). After Ti/Pt sputtered, the SU-8 was removed by acetone and sonicator for lift-off process (Figure 2.6 (k)). After the top electrode was formed, nonconductive epoxy (EPO-TEK 301, Epoxy Technology Inc, USA) was deposited for making a supporting layer (Figure 2.6 (l)). The nonconductive epoxy was cured at room temperature for 24 hours (Figure 2.6 (m)).

The figure 2.8 shows the fabricated PMN-PZT based Tm-pMUT array. In order to compare the cross talk, the PMN-PZT based Tm-pMUT array was fabricated two types, kerfed and kerfless. The kerfless type PMN-PZT based Tm-pMUT array was fabricated without ICP etching but just had patterned top electrodes.

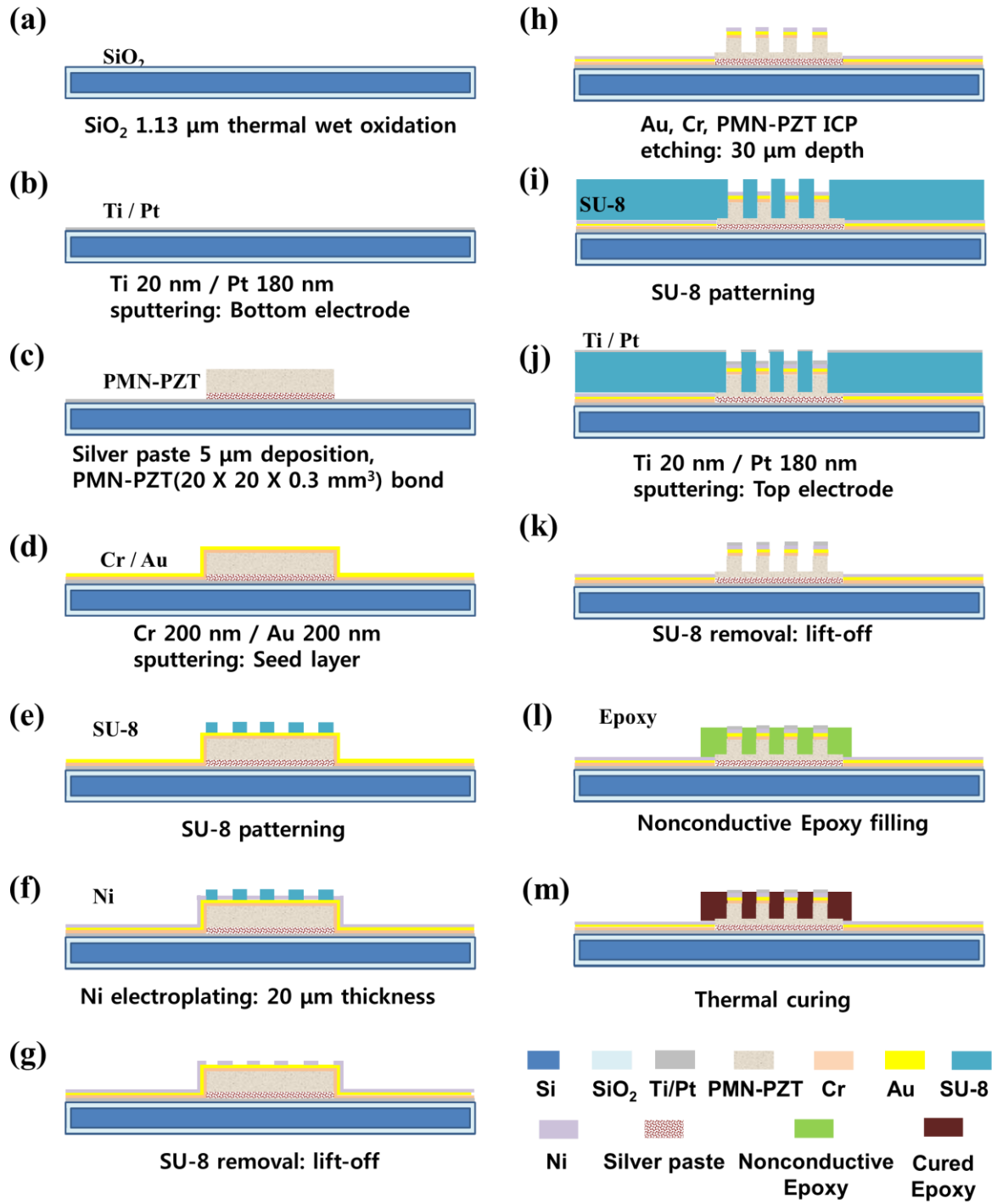


**Figure 2.6** Fabrication process of the PMN-PZT based Tm-pMUT array: (a)  $\text{SiO}_2$  was deposited by thermal wet oxidation, (b) Ti/Pt was sputtered for bottom electrode, (c) silver paste was deposited for PMN-PZT adhesion, (d) Cr/Au was sputtered for seed layer, (e) SU-8 was patterned by photolithography for Ni patterning, (f) Ni was electroplated for hard mask, (g) SU-8 removal for lift-off, (h) Au/Cr/PMN-PZT was etched by Metal ICP-RIE system, (i) SU-8 was patterned by photolithography for top electrode patterning, (j) Ti/Pt was sputtered for top electrode, (k) SU-8 removal for lift-off, (l) Nonconductive epoxy was deposited for making a supporting layer, (m) Nonconductive epoxy was thermally cured.

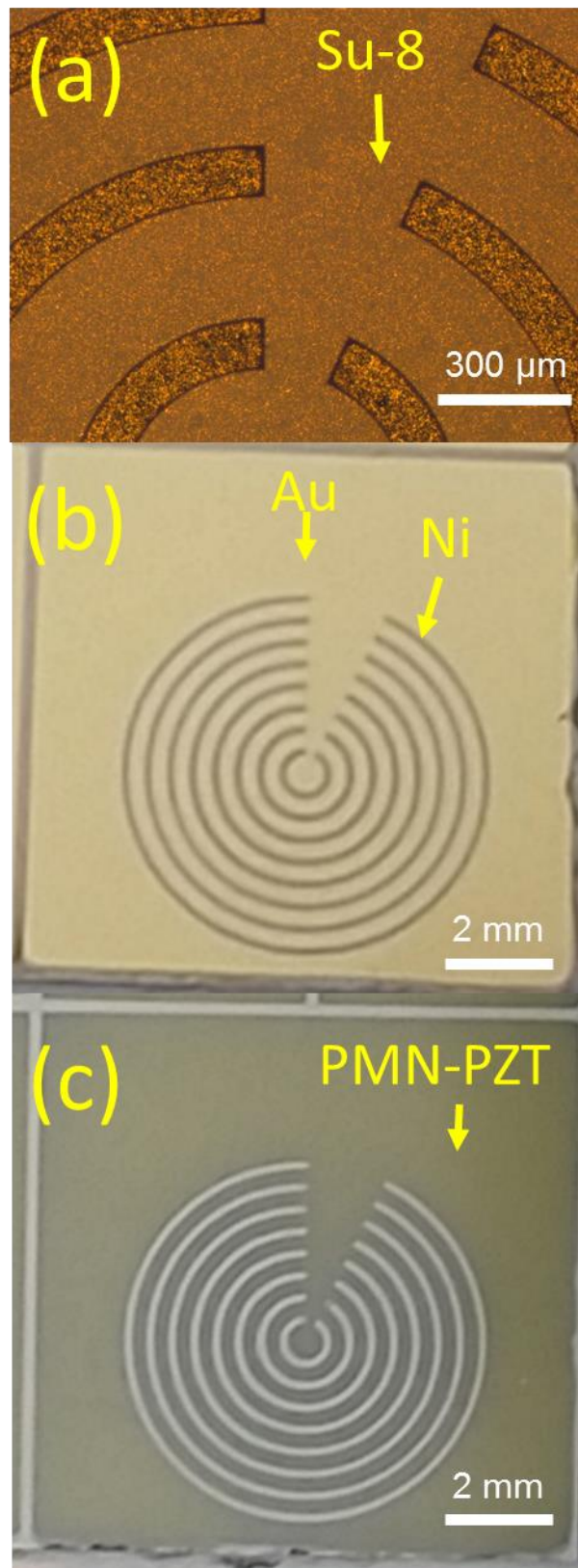


**Figure 2.7** Optical images of PMN-PZT based Tm-pMUT array after (a) SU-8 patterned (b) Ni electroplated (c) ICP etched.

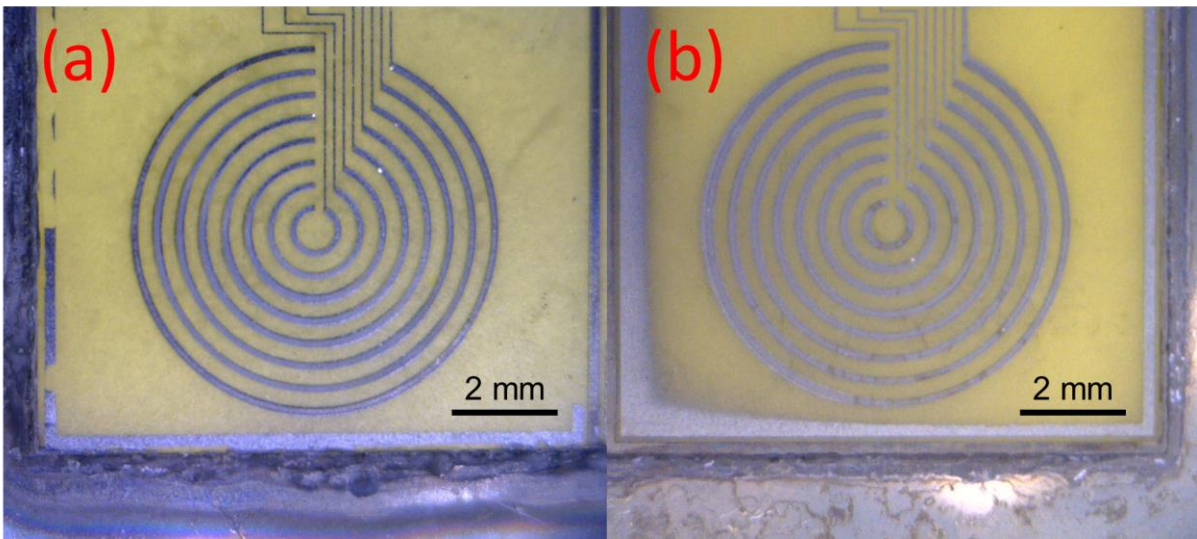


**Figure 2.8 Fabricated PMN-PZT based Tm-pMUT array (a) kerfed type PMN-PZT based Tm-pMUT array (b) kerfless type PMN-PZT based Tm-pMUT array.**

### 3. Experiment

#### 3.1 Impedance analysis of the PMN-PZT based Tm-pMUT array

The fabricated PMN-PZT based Tm-pMUT array was  $k_{33}$  mode type. The PMN-PZT based Tm-pMUT array working on 3 direction (thickness direction) dominantly when the device was applied AC voltage.

To measure the impedance of PMN-PZT based Tm-pMUT array, the poling was processed. The fabricated PMN-PZT based Tm-pMUT array were poled at a room temperature by applying a DC field of 2kV/mm for 2 hours by ferroelectric test system in the probe station (Figure 3.1). After poling process, the resonance frequency of PMN-PZT based Tm-pMUT array was measured by impedance analyzer (4294A, Agilent Technology, USA) in the probe station to reduce external noise (Figure 3.2).

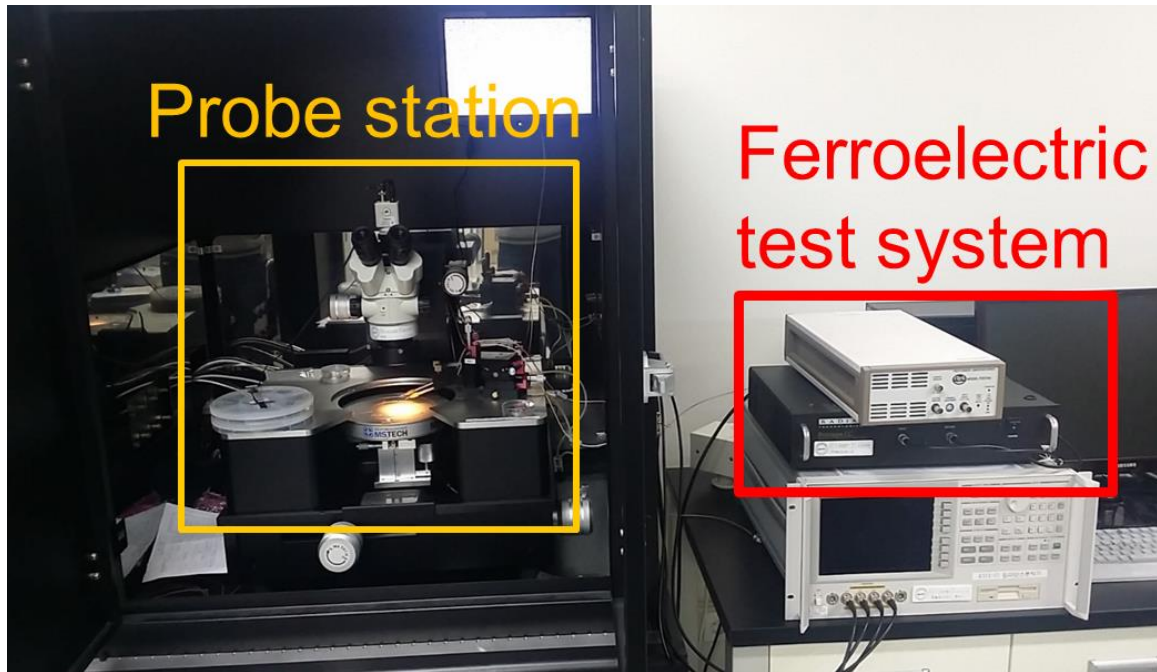
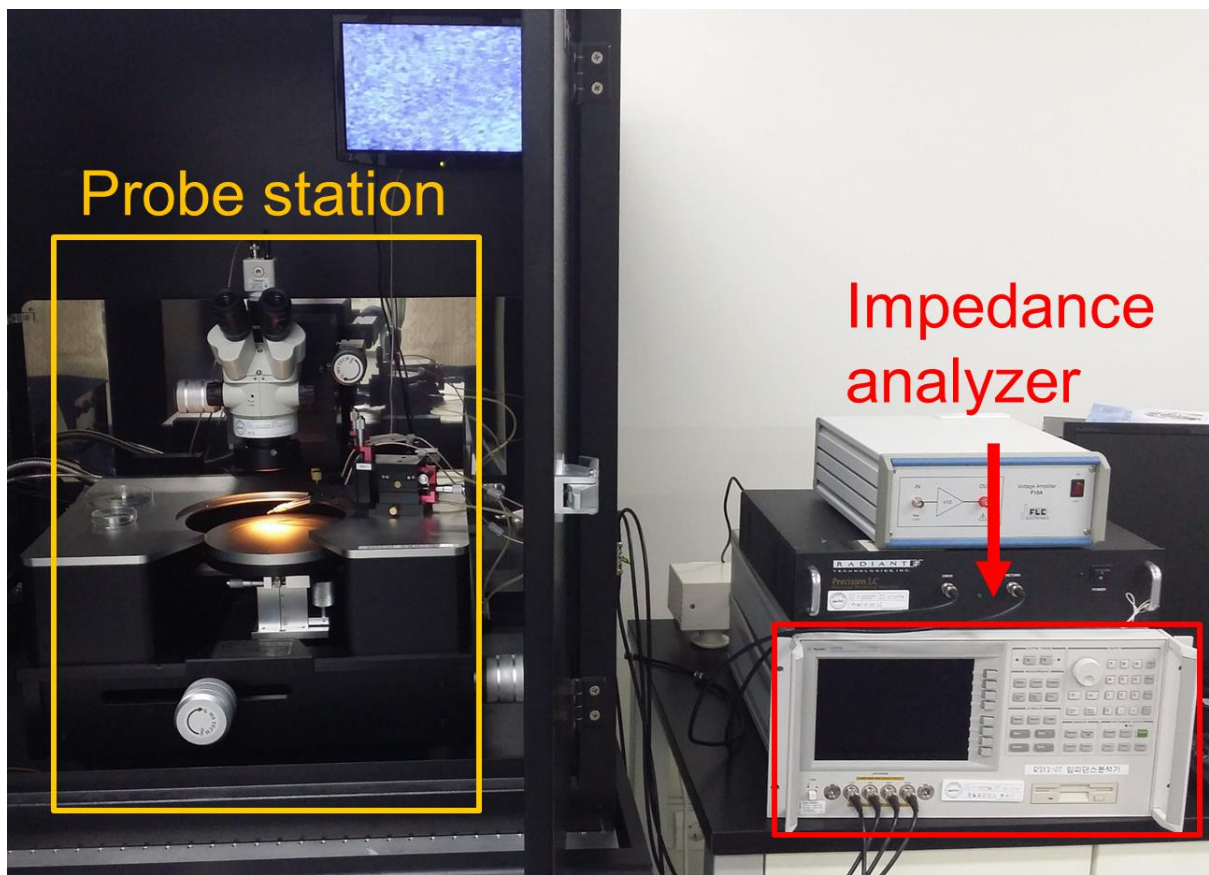


Figure 3.1 Optical image of ferroelectric test system.



**Figure 3.2 Optical image of impedance analyzer and probe station.**



## 4. Results and Discussions

### 4.1 PMN-PZT ICP etching results

#### 4.1.1 The etch rate and etch selectivity ratio results of PMN-PZT/Ni

The etching characteristics of PMN-PZT single crystal may have mixture behaviors of PMN and PZT, because the PMN-PZT consist of Pb, Mg, Nb, Ti, Zr, O elements.

The figure 4.1 indicated the etch rate and etch selectivity ratio of PMN-PZT/Ni as a function of  $\text{Cl}_2/\text{Ar}$  gas mixing ratio. The proportion of  $\text{Cl}_2$  gas was varied from 0 % to 100 %. The chamber pressure, RF power, ICP bias power, and total gas flow rate were fixed 2 mTorr, 600 W, 250 W, and 20 sccm, respectively. The maximum etch rate was 73.65 nm/min at  $\text{Cl}_2/\text{Ar}=7/3$  gas mixing ratio. Those ICP etching conditions gave a 3.35 etch selectivity ratio. Generally, the  $\text{Cl}_2$  was important chemical etching factor of metal [57]. When  $\text{Cl}_2$  mixing ratio was over 70 %, the etch rate was decreased. The  $\text{Ar}^+$  ion was considered as important etching factor of physical etching. After the PMN-PZT single crystal was etched, the  $\text{PbCl}_x$ ,  $\text{NbCl}_x$ ,  $\text{TiCl}_x$  were produced by etch product.

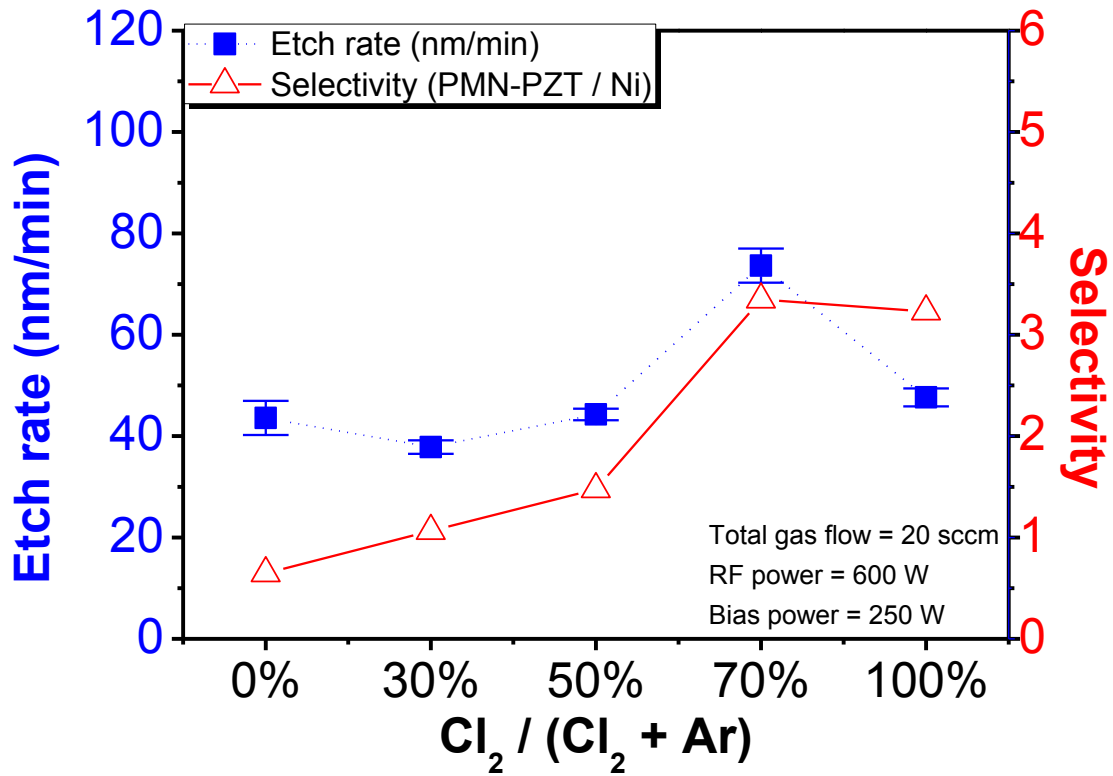


Figure 4.1 Etch rate and etch selectivity ratio of PMN-PZT as a function of  $\text{Cl}_2/\text{Ar}$  gas mixing ratio.

Table 4.1 Etch rate and etch selectivity ratio of PMN-PZT/Ni as a function of  $\text{Cl}_2/\text{Ar}$  gas mixing ratio.

Run No.		a-1	a-2	a-3	a-4	a-5	
RF power		W	600				
Bias power		W	250				
Gas flow rate (sccm)		Total	20				
		BCl <sub>3</sub>	0				
		Cl <sub>2</sub>	0	6	10	14	20
		Ar	20	14	10	6	0
Working pressure		mT	2				
Etching time		min	5				
Mask		Ni					
Etch rate	nm/min	PMN-PZT	43.59	37.85	44.28	73.65	47.64
		Standard Deviation(s)	3.35	1.33	1.13	3.37	1.78
		Ni	67.43	35.57	29.98	22.01	14.75
		Standard Deviation(s)	3.09	1.47	1.61	3.72	1.89
selectivity		0.65	1.06	1.48	3.35	3.23	



The figure 4.2 indicated the etch rate and etch selectivity ratio of PMN-PZT/Ni as a function of  $\text{BCl}_3/\text{Ar}$  gas mixing ratio. The proportion of  $\text{BCl}_3$  gas was varied from 0 % to 100 %. The chamber pressure, RF power, ICP bias power and total gas flow rate were fixed 2 mTorr, 600 W, 250 W, and 20 sccm, respectively. The maximum etch rate was 78.38 nm/min at  $\text{BCl}_3/\text{Ar} = 7/3$  gas mixing ratio. Those ICP etching condition gave a 3.65 etch selectivity ratio. The  $\text{BCl}_3$  was reported that can increase etch rate and etch selectivity ratio by B-O and BCl-O chemical bonding [58, 59]. The etch rate was maximized at 70 %  $\text{BCl}_3$  mixing ratio. The  $\text{Ar}^+$  ion was considered the effective removing factor of the nonvolatile etch product [60, 61]. The  $\text{B}^+$  and  $\text{BCl}^+$  broke the oxygen bond of PMN-PZT single crystal and recombined as B-O and BCl-O by chemical reaction.

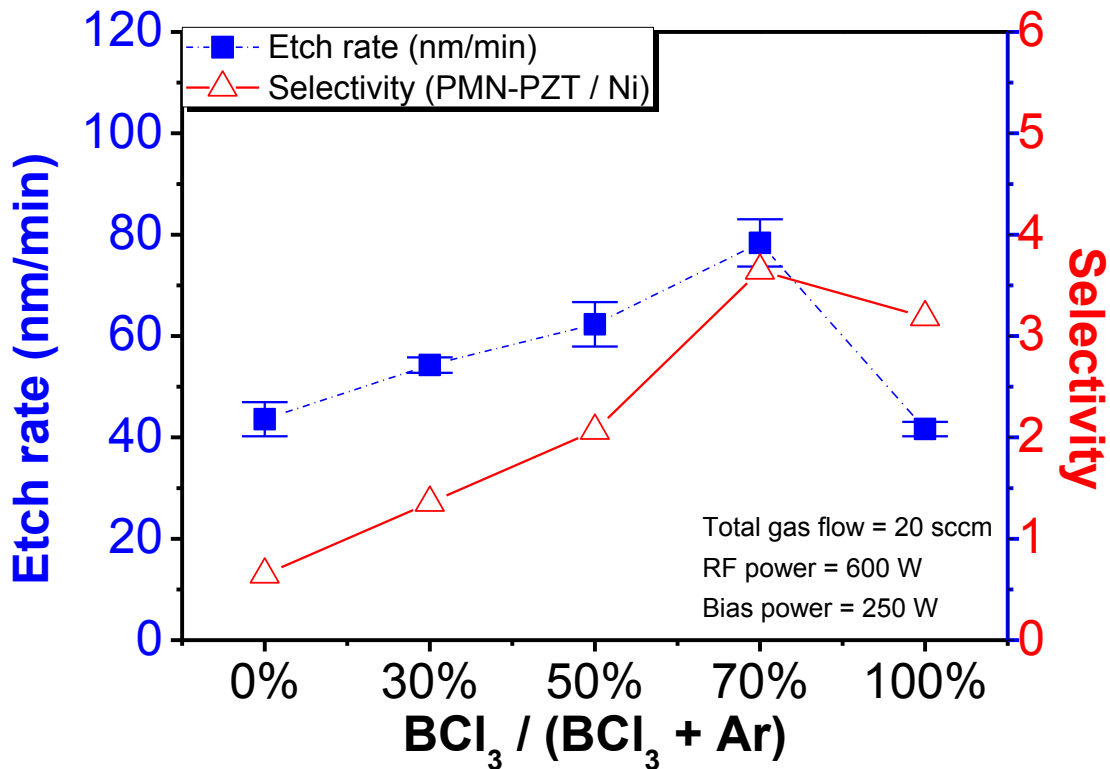


Figure 4.2 Etch rate and etch selectivity ratio of PMN-PZT as a function of  $\text{BCl}_3/\text{Ar}$  gas mixing ratio.

**Table 4.2 Etch rate and etch selectivity ratio of PMN-PZT as a function of BCl<sub>3</sub>/Ar gas mixing ratio.**

Run No.		b-1	b-2	b-3	b-4	b-5	
RF power		W					
Bias power		W					
Gas flow rate (sccm)	Total	20					
	BCl <sub>3</sub>	0	6	10	14	20	
	Cl <sub>2</sub>	0					
	Ar	20	14	10	6	0	
Working pressure		mT					
Etching time		min					
Mask		Ni					
Etch rate	nm/min	PMN-PZT	43.59	54.27	62.32	78.38	41.65
		Standard Deviation(s)	3.35	1.52	4.38	4.67	1.41
		Ni	67.43	40.03	30.18	21.50	13.07
		Standard Deviation(s)	3.09	1.09	4.08	2.48	1.71
selectivity		0.65	1.36	2.07	3.65	3.19	

The figure 4.3 indicated the etch rate and etch selectivity ratio of PMN-PZT/Ni as a function of BCl<sub>3</sub>/Cl<sub>2</sub>/Ar gas mixing ratio. The proportion of BCl<sub>3</sub> gas was varied from 0 % to 70 %. The Ar mixing ratio, chamber pressure, RF power, ICP bias power and total gas flow rate were fixed 30 %, 2 mTorr, 600 W, 250 W and 20 sccm, respectively. The maximum etch rate was 87.52 nm/min at BCl<sub>3</sub>/Cl<sub>2</sub>/Ar= 5/2/3 gas mixing ratio. Those ICP conditions gave a 4.12 etch selectivity ratio. The B<sup>+</sup> and BCl<sup>+</sup> ions broke the oxygen chemical bond of PMN-PZT single crystal and recombined as B-O and BCl-O by chemical reaction. The result showed that the BCl<sub>3</sub> plasma increased etch selectivity ratio without decreasing etch rate of PMN-PZT single crystal.

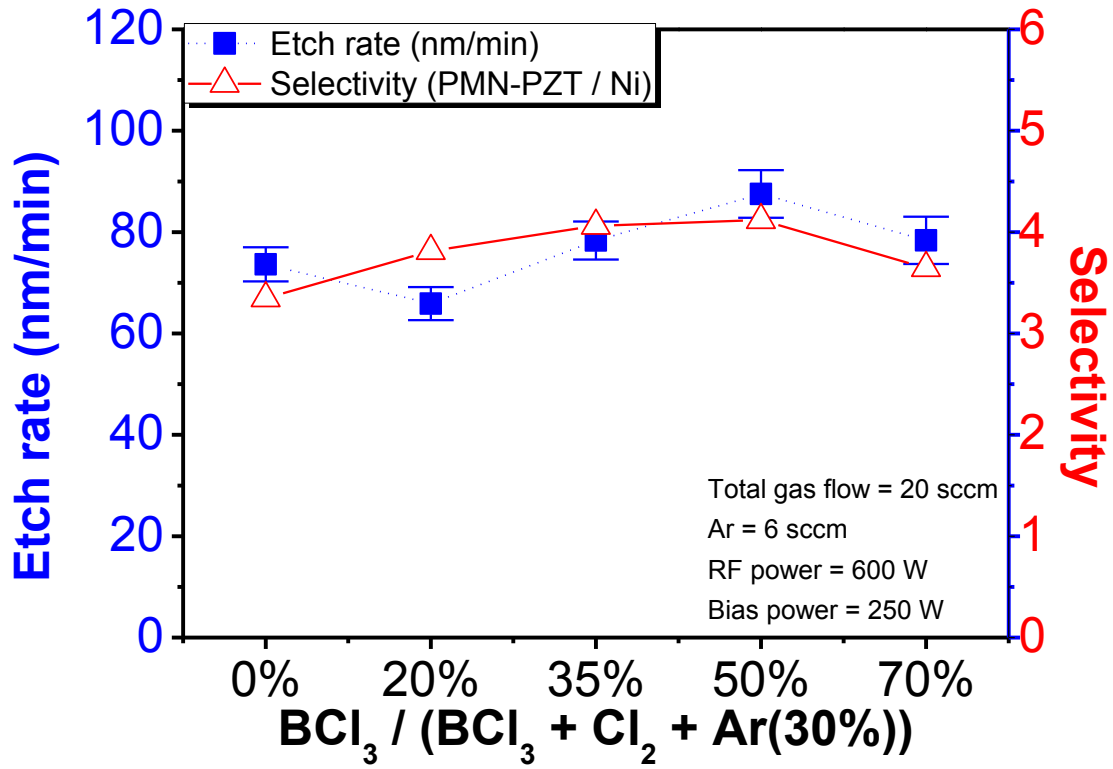


Figure 4.3 Etch rate and etch selectivity ratio of PMN-PZT as a function of BCl<sub>3</sub>/Cl<sub>2</sub>/Ar gas mixing ratio.

Table 4.3 Etch rate and etch selectivity ratio of PMN-PZT as a function of BCl<sub>3</sub>/Cl<sub>2</sub>/Ar gas mixing ratio.

Run No.		c-1	c-2	c-3	c-4	c-5	
RF power		W	600				
Bias power		W	250				
Gas flow rate (sccm)		Total	20				
		BCl <sub>3</sub>	0	4	7	10	14
		Cl <sub>2</sub>	14	10	7	4	0
		Ar	6				
Working pressure		mT	2				
Etching time		min	5				
Mask		Ni					
Etch rate	nm/min	PMN-PZT	73.65	65.89	78.34	87.52	78.38
		Standard Deviation(s)	3.37	3.26	3.76	4.70	4.67
		Ni	22.01	17.28	19.28	21.25	21.50
		Standard Deviation(s)	3.72	2.29	3.64	4.53	2.48
selectivity		3.35	3.81	4.06	4.12	3.65	

The figure 4.4 shows the etch rate and etch selectivity ratio of PMN-PZT/Ni as a function of RF power. The RF power was varied from 200 W to 1000 W. The gas mixing ratio, chamber pressure, and ICP bias power were fixed  $\text{BCl}_3/\text{Cl}_2/\text{Ar} = 5/2/3$  (10/4/6 sccm), 2 mTorr, and 250 W, respectively. The maximum etch rate was 90.37 nm/min at 800 W RF power. The etch selectivity ratio was 4.77 at those ICP etching conditions. The RF power was considered the important factor of making ions. So the chemical reaction was increased along the increase of ion production. However, overmany ions decreased the etch rate and etch selectivity ratio. Because the mean free path was decreased and the nonvolatile etch product was increased.

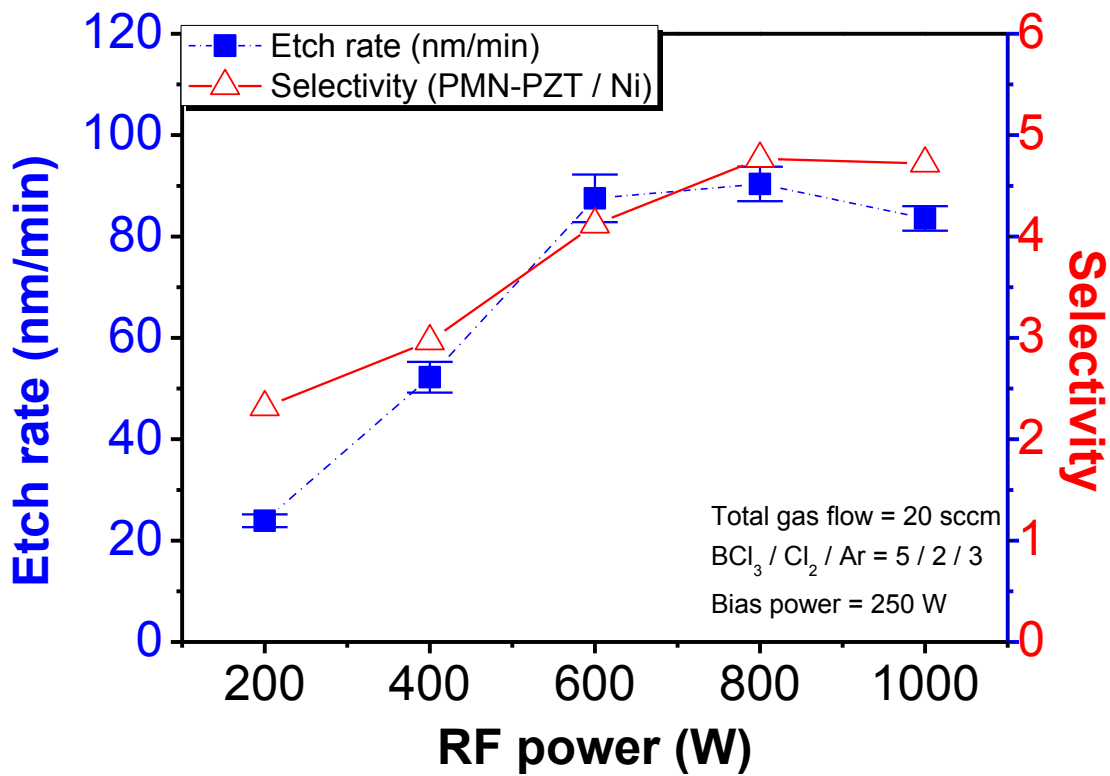


Figure 4.4 Etch rate and etch selectivity ratio of PMN-PZT as a function of RF power.

**Table 4.4 Etch rate and etch selectivity ratio of PMN-PZT as a function of Cl<sub>2</sub>/Ar gas mixing ratio.**

Run No.		d-1	d-2	d-3	d-4	d-5	
RF power	W	200	400	600	800	1000	
Bias power	W	250					
Gas flow rate (sccm)	Total	20					
	BCl <sub>3</sub>	10					
	Cl <sub>2</sub>	4					
	Ar	6					
Working pressure	mT	2					
Etching time	min	5					
Mask		Ni					
Etch rate	nm/min	PMN-PZT	23.92	52.23	87.52	90.37	83.57
		Standard Deviation(s)	1.26	3.04	4.70	3.41	2.42
		Ni	10.32	17.60	21.25	18.96	17.70
		Standard Deviation(s)	3.13	1.09	4.53	4.94	4.02
selectivity		2.32	2.97	4.12	4.77	4.72	

The figure 4.5 shows the etch rate and etch selectivity ratio of PMN-PZT/Ni as a function of Bias power. The bias power was varied from 50 W to 450 W. The gas mixing ratio, chamber pressure, and RF power were fixed BCl<sub>3</sub>/Cl<sub>2</sub>/Ar= 5/2/3 (10/4/6 sccm), 2 mTorr, 600 W, respectively. The optimum etch rate was 101.35 nm/min at 350 W Bias power. Those ICP etching conditions gave a 3.95 etch selectivity ratio. The bias power was determined the collision energy of ions. So, the etch selectivity ratio was decreased along the increase of the bias power. The bias power was important factor of the physical etching. The figure 4.5 indicated that the physical etching was dominant than the chemical etching.

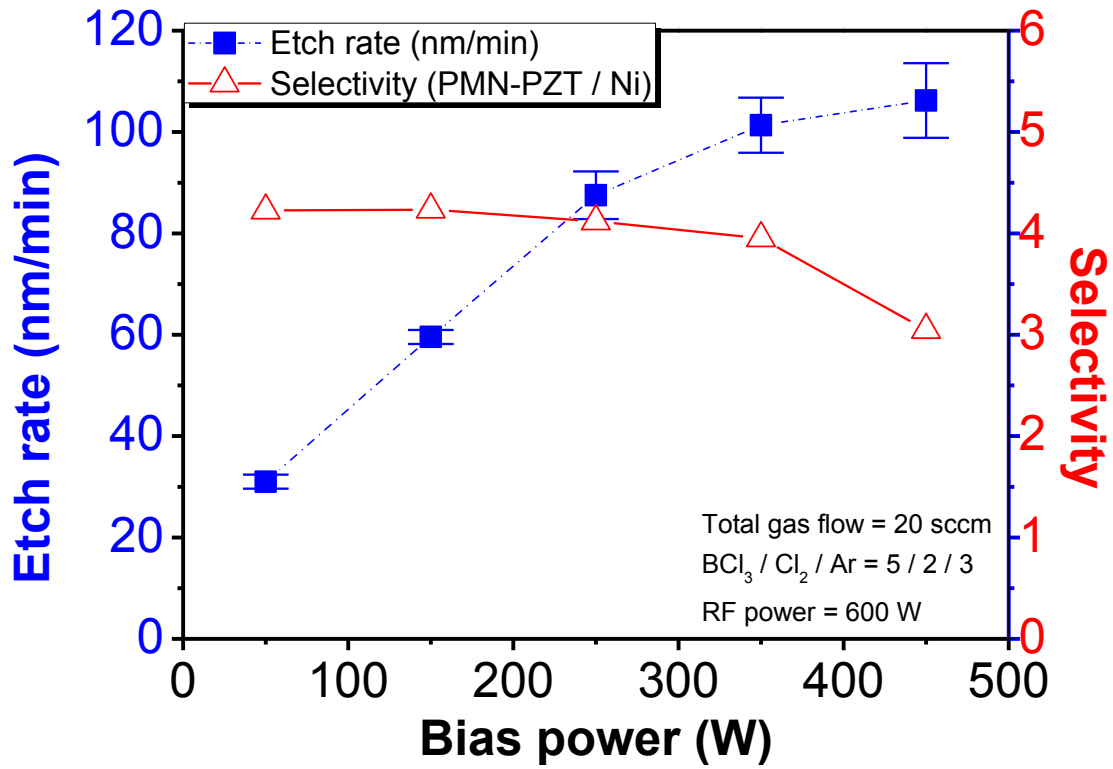


Figure 4.5 Etch rate and etch selectivity ratio of PMN-PZT as a function of Bias power.

Table 4.5 Etch rate and etch selectivity ratio of PMN-PZT as a function of Bias power.

Run No.		e-1	e-2	e-3	e-4	e-5
RF power	W	600				
Bias power	W	50	150	250	350	450
Gas flow rate (sccm)	Total	20				
	BCl <sub>3</sub>	10				
	Cl <sub>2</sub>	4				
	Ar	6				
Working pressure	mT	2				
Etching time	min	5				
Mask		Ni				
Etch rate	PMN-PZT	31.01	59.56	87.52	101.35	106.22
	Standard Deviation(s)	1.39	1.37	4.70	5.45	7.36
	Ni	7.34	14.07	21.25	25.65	34.87
	Standard Deviation(s)	1.78	2.39	4.53	3.97	5.57
selectivity		4.23	4.23	4.12	3.95	3.05

The figure 4.6 shows the comparison PMN-PZT single crystal etching results for RF power, Bias power and combination of optimized parameters. The optimized condition was  $\text{BCl}_3/\text{Cl}_2/\text{Ar}= 5/2/3$  (10/4/6 sccm), 800 W RF power, 350 W bias power, 2 mTorr chamber pressure. Those ICP etching conditions gave a 107.6 nm/min etch rate and 4.22 etch selectivity ratio. It means that the physical etching was dominant and the chemical etching helps the physical etching.

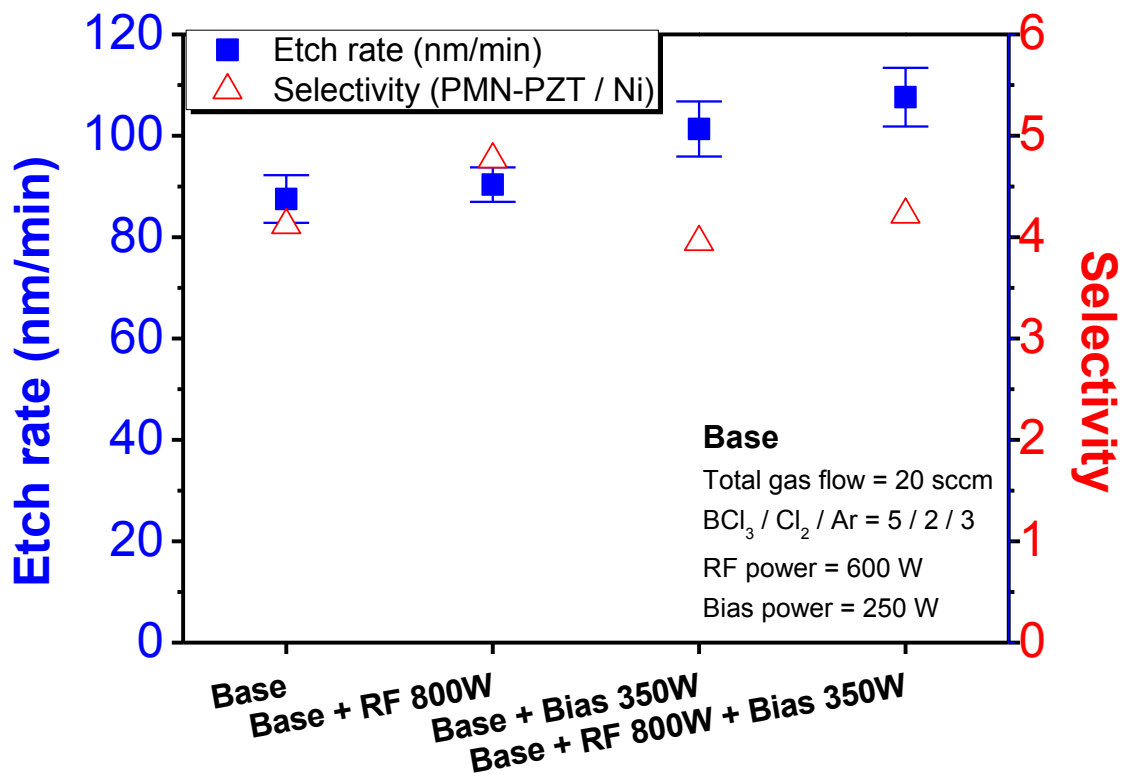


Figure 4.6 Comparative PMN-PZT etching results for RF power, Bias power and combination of optimized parameters.

**Table 4.6 Comparative PMN-PZT etching results for RF power, Bias power and combination of optimized parameters.**

Run No.		c-4	d-4	e-4	F	
RF power		W	600	800	600	800
Bias power		W	250	250	350	350
Gas flow rate (sccm)		Total	20			
		BCl <sub>3</sub>	10			
		Cl <sub>2</sub>	4			
		Ar	6			
Working pressure		mT	2			
Etching time		min	5			
Mask		Ni				
Etch rate	nm/min	PMN-PZT	87.52	90.37	101.35	107.62
		Standard Deviation(s)	4.70	3.41	5.45	5.80
		Ni	21.25	18.96	25.65	25.49
		Standard Deviation(s)	4.53	4.94	3.97	3.61
selectivity		4.12	4.77	3.95	4.22	



#### 4.1.2 Effect of bias power on the sidewall angle of PMN-PZT single crystal

The figure 4.5 presented the bias power was important factor of etch rate. So, the sidewall angle of PMN-PZT single crystal was investigated based on bias power. The figure 4.7 shows scanning electron microscope (SEM) micrographs of etched PMN-PZT single crystal at various bias power. The bias power was varied from 250 W to 450 W. The gas mixing ratio, chamber pressure, and RF power were fixed  $\text{BCl}_3/\text{Cl}_2/\text{Ar}= 5/2/3$  (10/4/6 sccm), 2 mTorr, and 600 W, respectively. The sidewall angles were increased along the increase of the bias power. In conclusion, the high bias power was a necessary in order to get a vertical structure.

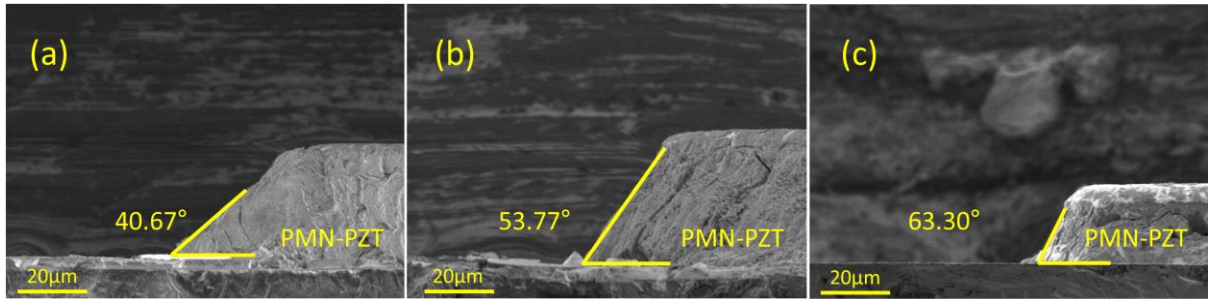


**Figure 4.7 SEM micrographs of etched PMN-PZT single crystal at (a) 250 W bias power, (b) 350 W bias power and (c) 450 W bias power.**

#### 4.1.3 The X-ray photoelectron spectroscopy (XPS) analysis results of PMN-PZT single crystal

The figure 4.8 to figure 4.11 indicated the XPS results at non-etched PMN-PZT single crystal, etched PMN-PZT single crystal in  $\text{Cl}_2/\text{Ar}= 7/3$  (14/6 sccm) gas mixing ratio, etched in  $\text{BCl}_3/\text{Ar}= 7/3$  (14/6 sccm) gas mixing ratio and etched in  $\text{BCl}_3/\text{Cl}_2/\text{Ar}= 5/2/3$  (10/4/6 sccm) gas mixing ratio. The chamber pressure, RF power, and Bias power were fixed 2 mTorr, 600 W, and 350 W respectively.

The Pb 4f spectra can be resolved into Pb-O, Pb- $\text{Cl}_x$ , and Pb. The peak at 137.6, 138.9 eV binding energies correspond to PbO, Pb- $\text{Cl}_x$  [62, 63]. It was evidence that the chemical bond of Pb-O was broken to react with Cl gas and the peak of metal Pb in the Pb 4f peak begun to appear upon etching, decreased the Pb content. The Pb-O peaks relatively lowered in  $\text{BCl}_3/\text{Cl}_2/\text{Ar}= 5/2/3$  (10/4/6 sccm) plasma condition. After the PMN-PZT single crystal was etched, the core binding energy of Pb 4f was shifted to high as  $\Delta x$  ( $=0.7$  eV).

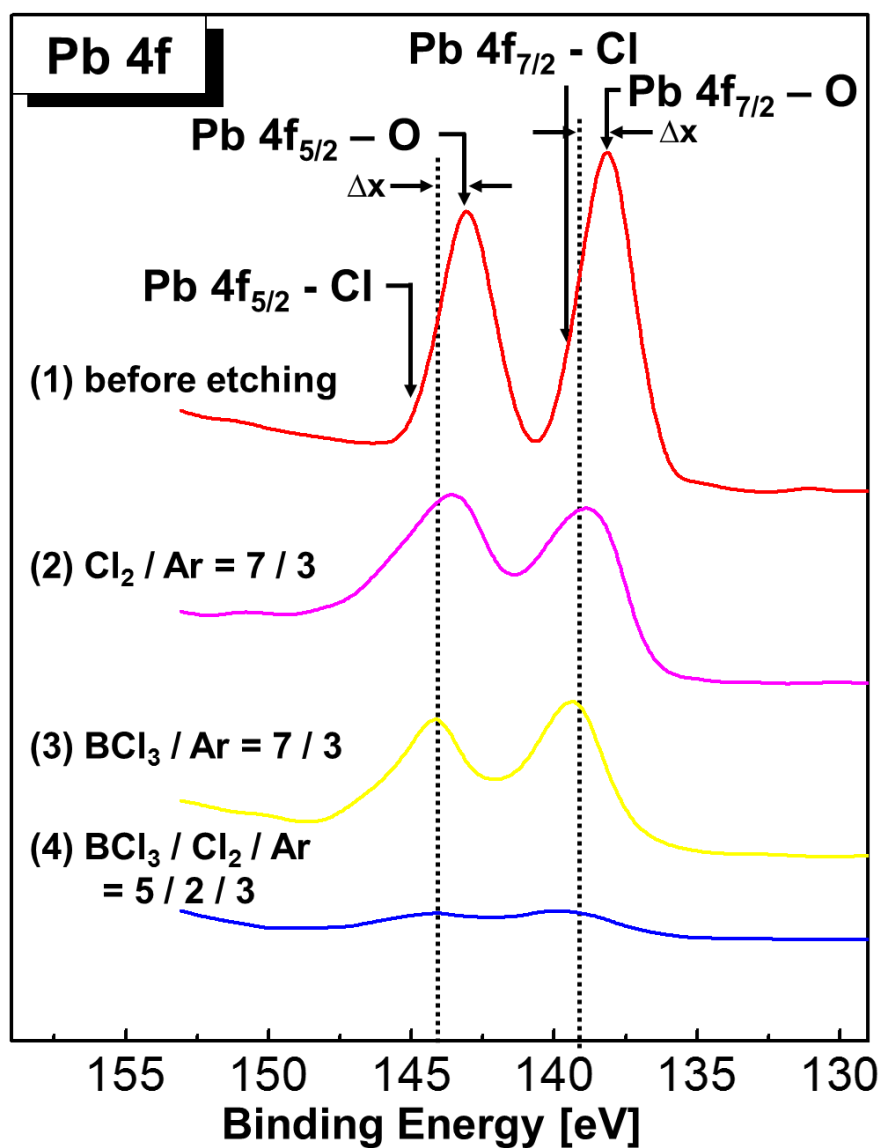


Figure 4.8 XPS spectra of Pb 4f as variations of BCl<sub>3</sub>/Cl<sub>2</sub>/Ar gas mixing ratio.

The Zr 3d spectra can be resolved into Zr-O, Zr- Cl. The peak at 183.3, 184.5 eV binding energies correspond to Zr-O, Zr- Cl. [64, 65].

The intensity of the Zr-O peaks was the highest in the condition of Cl<sub>2</sub>/Ar= 7/3 (14/6 sccm) gas mixing ratio. Therefore, the etch rate was the lowest in that gas mixture. On the other

hand, the intensity of the Zr-O peak was lowest in  $\text{BCl}_3/\text{Cl}_2/\text{Ar} = 5/2/3$  (10/4/6 sccm) gas mixing ratio. After the PMN-PZT single crystal was etched, the core binding energy of Zr 3d was shifted to high as  $\Delta y$  ( $=0.5$  eV).

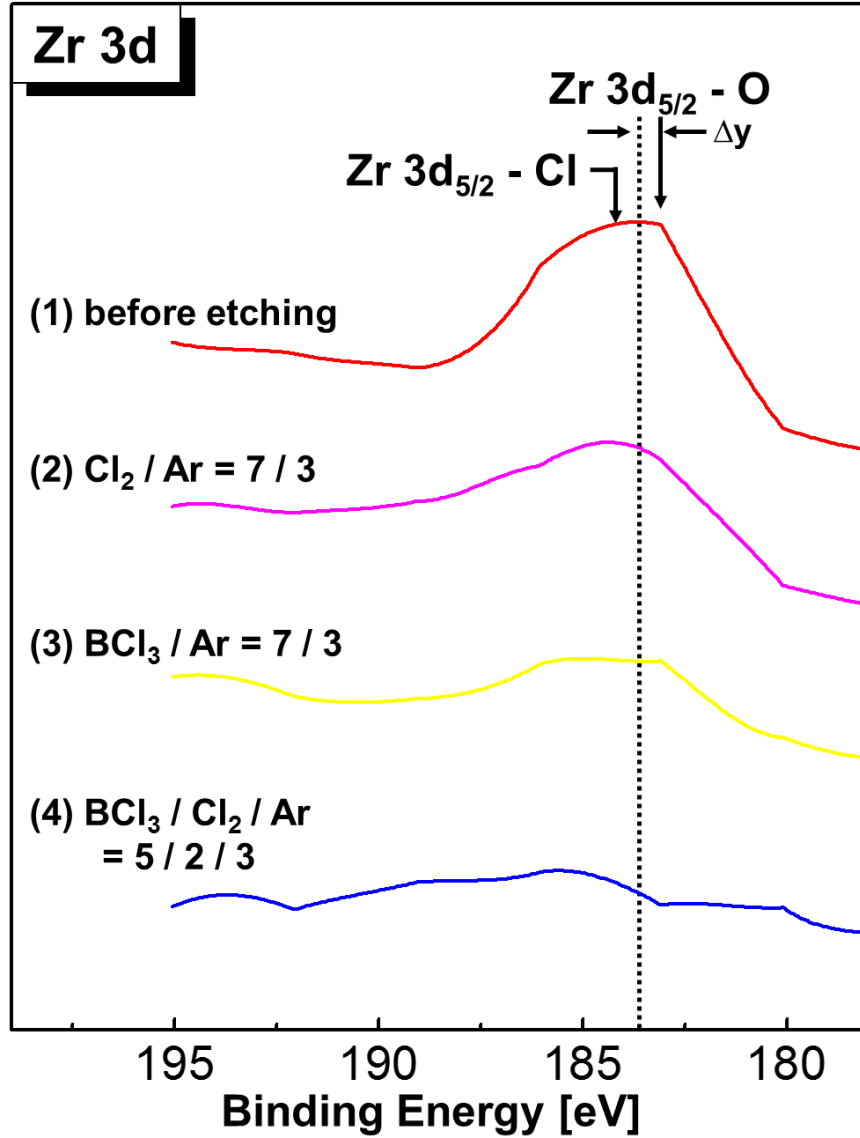


Figure 4.9 XPS spectra of Zr 3d as variations of  $\text{BCl}_3/\text{Cl}_2/\text{Ar}$  gas mixing ratio.

The Ti 2p spectra can be resolved into Ti-O, Ti-Cl. The peak at 458.5, 459.5 eV binding energies correspond to Ti-O, Ti-Cl [66, 67]. The Ti-O peak shifted to high binding energy by as much as  $\Delta z$  ( $= 0.8$  eV). The intensity of the Ti-O peak was lowest in  $\text{BCl}_3/\text{Cl}_2/\text{Ar} = 5/2/3$  (10/4/6 sccm) gas mixing ratio.

The Nb 3s spectra can be resolved into Nb-O, Nb-Cl. The peak at 470.8 eV binding energy correspond to Nb-O [68]. After the PMN-PZT single crystal was etched, the binding energy of Nb-Cl was observed at 474.0 eV. The intensity of the Nb-O peak was lowest in  $\text{BCl}_3/\text{Cl}_2/\text{Ar} = 5/2/3$  (10/4/6 sccm) gas mixing ratio.

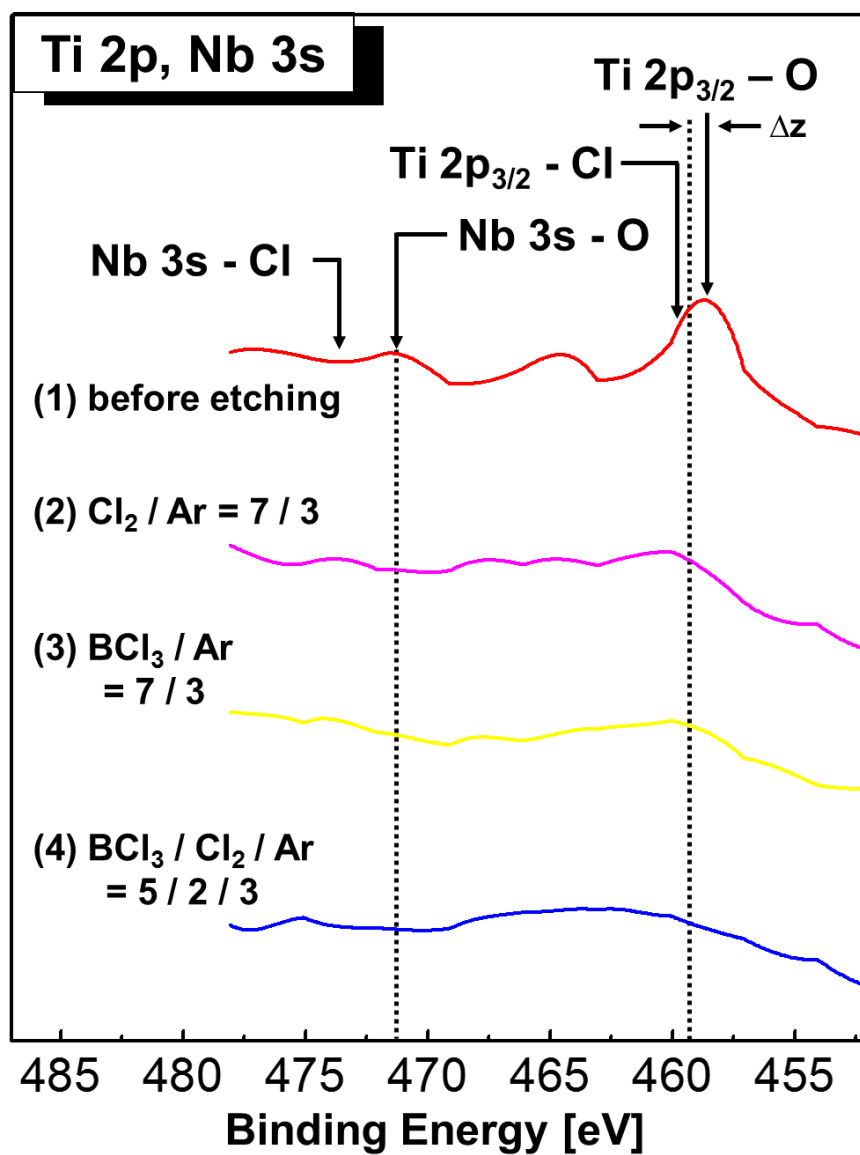


Figure 4.10 XPS spectra of Ti 2p and Nb 3s as variations of BCl<sub>3</sub>/Cl<sub>2</sub>/Ar gas mixing ratio.

The Mg 1s spectra can be resolved into Mg-O, Mg-Cl. The binding energies of Mg-O and Mg-Cl were observed at 1306.0 and 1307.5 eV. The intensity of the Mg-O peaks were the highest in the condition of Cl<sub>2</sub>/Ar=7/3 (14/6 sccm) gas mixing ratio. Therefore, the etch rate

was the lowest in that gas mixture. On the other hand, the intensity of the Mg-O peak was lowest in  $\text{BCl}_3/\text{Cl}_2/\text{Ar} = 5/2/3$  (10/4/6 sccm) gas mixing ratio.

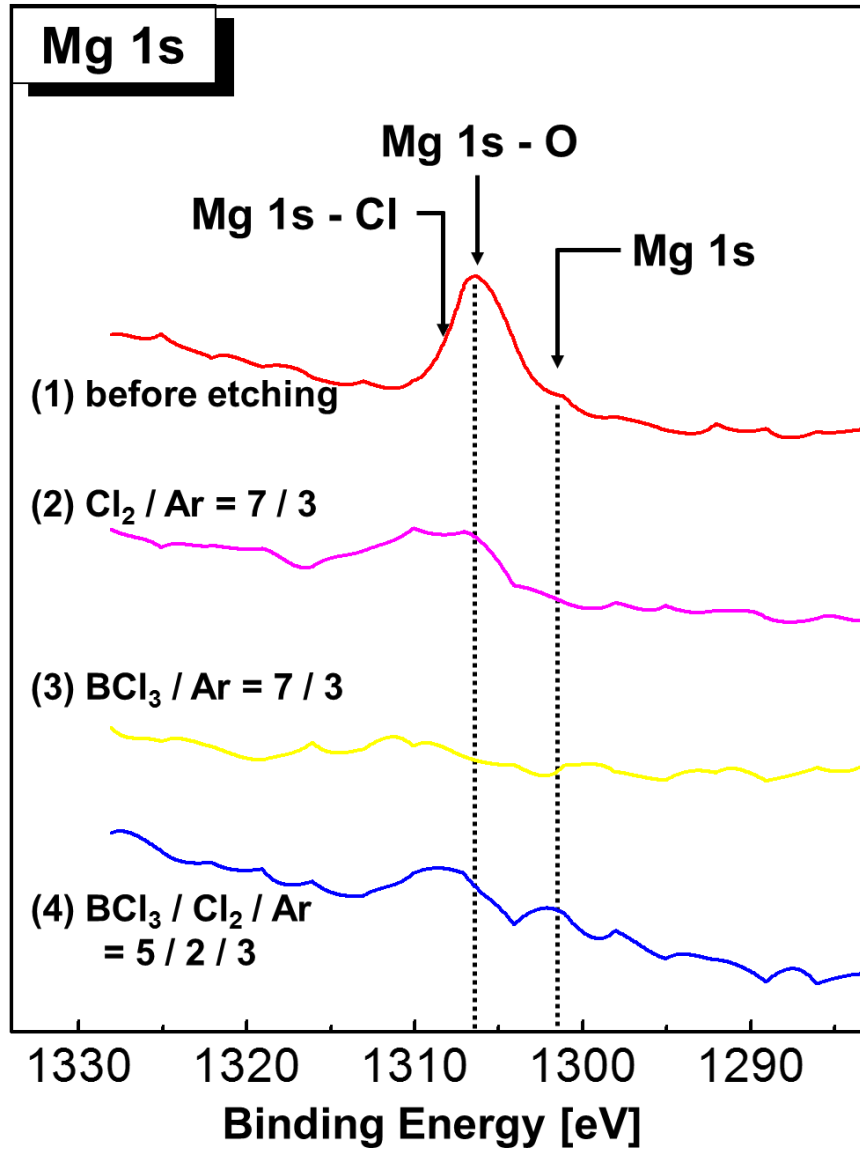


Figure 4.11 XPS spectra of Mg 1s as variations of  $\text{BCl}_3/\text{Cl}_2/\text{Ar}$  gas mixing ratio.

After the PMN-PZT single crystal was etched, the reason why the binding energy peak intensity was decreased due to physical etching by positive ions [69]. As a result, the

amorphous layer was produced on the PMN-PZT surface [70]. So, the binding energy peak intensity was decreased.



#### 4.1.4 Discussion of PMN-PZT ICP etching

In this research, the dry etching characteristics of PMN-PZT single crystal were investigated using ICP etching system. The  $\text{BCl}_3/\text{Cl}_2/\text{Ar}$  gas mixture was used to make plasma. The investigated process parameters were RF power, chamber pressure, bias power, gas mixing ratio. The ICP source power was varied from 200 W to 1000 W. chamber pressure, bias power and gas flow rate were controlled from 50 W to 450 W, 20 sccm. The optimized condition was  $\text{BCl}_3/\text{Cl}_2/\text{Ar} = 5/2/3$  (10/4/6 sccm), 800 W RF power, 350 W bias power, 2 mTorr chamber pressure. Those optimized ICP etching conditions gave a 107.6 nm/min etch rate and 4.22 etch selectivity ratio. The research showed that the  $\text{BCl}_3/\text{Cl}_2/\text{Ar}$  plasma increased etch selectivity ratio without decreasing etch rate of PMN-PZT single crystal. The XPS study performed on clean surface of the PMN-PZT after dry etched. XPS analysis revealed that  $\text{BCl}_3/\text{Cl}_2/\text{Ar} = 5/2/3$  (10/4/6 sccm) plasma was optimized ICP etching condition. The sidewall angles was increased along the increase of the bias power.

This results were expected to be used for making various transducers like cell stimulation system, IVUS transducer, high frequency ultrasonic transducer.

## **4.2 Electrical characterization of the PMN-PZT based Tm-pMUT array**

### **4.2.1 Impedance analyzing of the kerfed type PMN-PZT based Tm-pMUT array**

The figure 4.12 shows the impedance and phase of the kerfed type PMN-PZT based Tm-pMUT array. The measured impedance values were decreased along the increase of the elements number. Because the area of elements were increased along the increase of the elements number while the resistances were decreasing. The resonance frequencies of element No.1 to element No. 8 were 2.62 MHz to 2.68 MHz. The average resonance frequency was  $2.66 (\pm 0.04)$  MHz. The anti-resonance frequencies of element No. 1 to element No. 8 were 3.20 MHz to 3.18 MHz. The average anti-resonance frequency was  $3.18 (\pm 0.03)$  MHz. The resonance frequencies and anti-resonance frequencies were quite similar with each elements. Because the resonance frequency was determined by thickness of piezoelectric material [71]. The measured effective electromechanical coupling coefficient ( $k_{\text{eff}}^2$ ) was 30.05%.

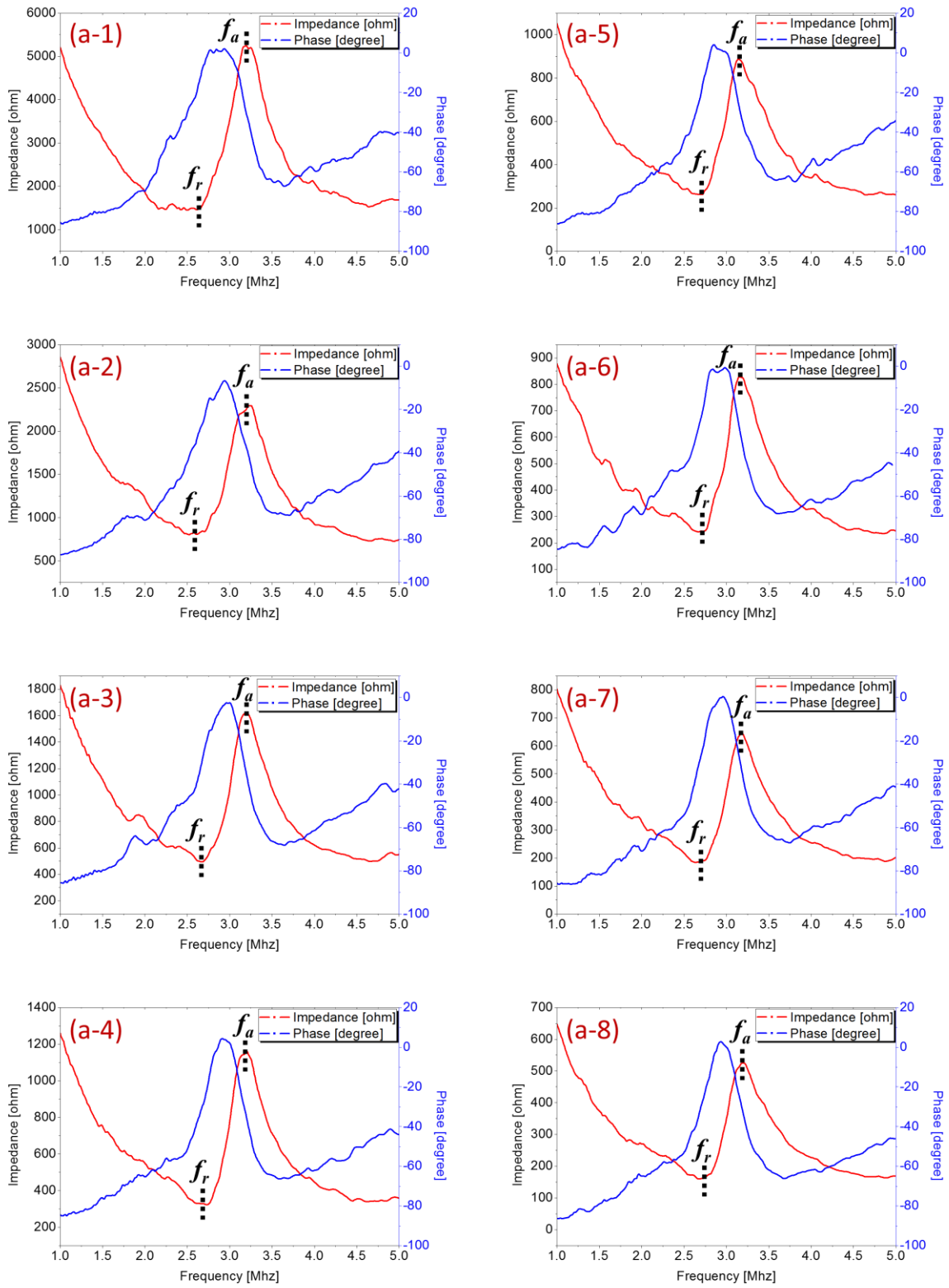


Figure 4.12 Impedance and phase analyzing results of the kerfed type PMN-PZT based Tm-pMUT array.

**Table 4.7 Electric characterization of the kerfed type PMN-PZT based Tm-pMUT array.**

Elements No.	$f_r$ [MHz]	$f_a$ [MHz]	$k_{eff}$	$k_{eff}^2$
a-1	2.62	3.20	0.57	32.96%
a-2	2.62	3.24	0.59	34.61%
a-3	2.66	3.20	0.56	30.90%
a-4	2.74	3.20	0.52	26.68%
a-5	2.68	3.14	0.52	27.15%
a-6	2.68	3.16	0.53	28.07%
a-7	2.64	3.18	0.56	31.08%
a-8	2.68	3.18	0.54	28.97%

#### **4.2.2 Impedance analyzing of the kerfless type PMN-PZT based Tm-pMUT array**

To identify difference with kerfed type, the kerfless type PMN-PZT based Tm-pMUT array was measured the impedance and phase by impedance analyzer. The figure 4.13 shows the results. The resonance frequencies of element No. 1 to element No. 8 were 2.68 MHz to 2.70 MHz. The average resonance frequency was  $2.69 (\pm 0.03)$  MHz. The anti-resonance frequencies of element No. 1 to element No. 8 were 3.14 MHz to 3.16 MHz. The average anti-resonance frequency was  $3.15 (\pm 0.02)$  MHz. The measured impedance values were decreased along the increase of the elements number. Because the area of elements were increased along the increase of the elements number while the resistances were decreased. It was same principle with kerfed type. The measured effective electromechanical coupling coefficient ( $k_{\text{eff}}^2$ ) was 26.89%.

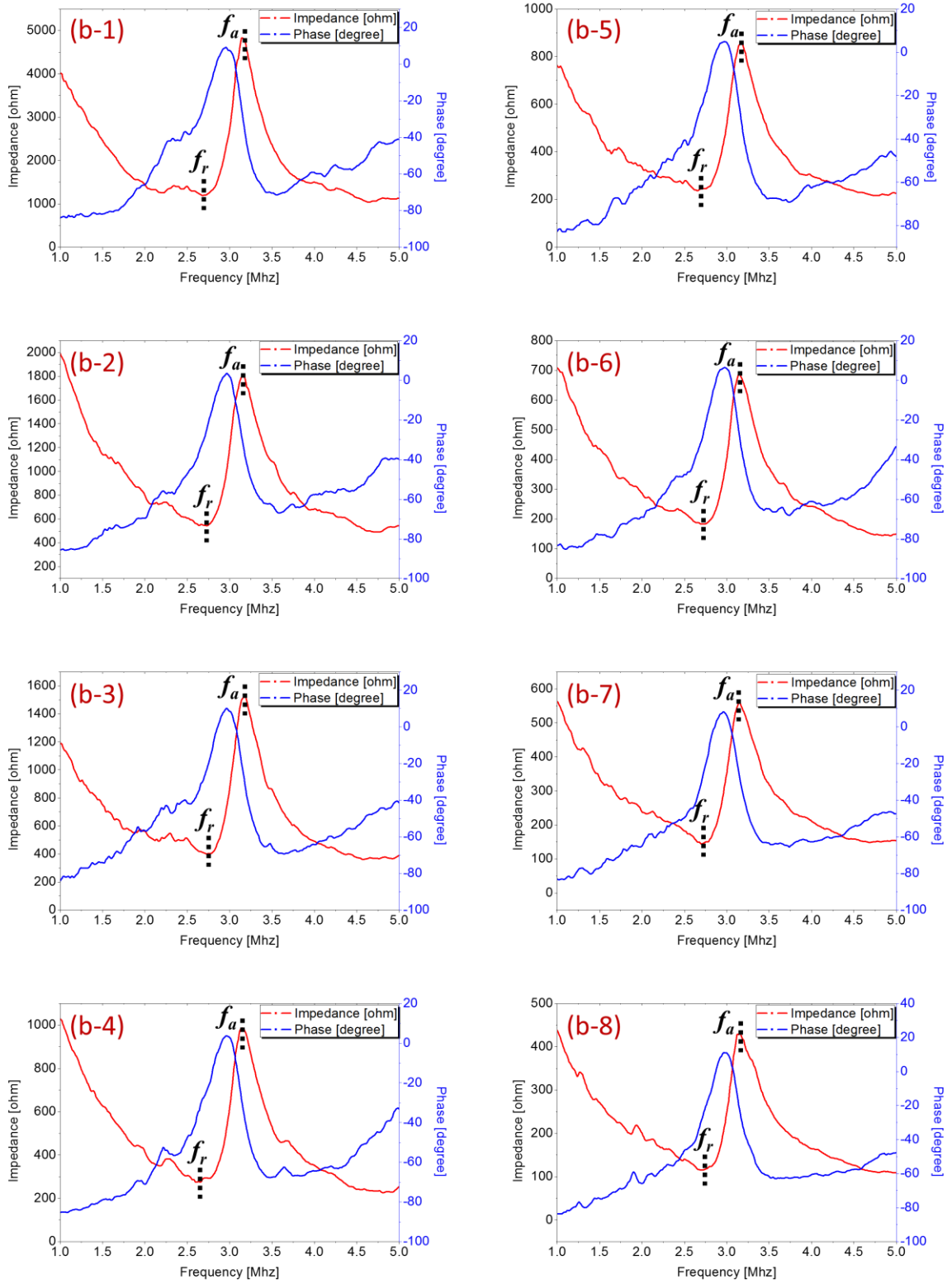


Figure 4.13 Impedance and phase analyzing results of the kerfless type PMN-PZT based Tm-pMUT array.

**Table 4.8 Electric characterization of the kerfless type PMN-PZT based Tm-pMUT array.**

Elements No.	$f_r$ [MHz]	$f_a$ [MHz]	$k_{eff}$	$k_{eff}^2$
b-1	2.68	3.14	0.52	27.15%
b-2	2.72	3.16	0.51	25.91%
b-3	2.74	3.18	0.51	25.76%
b-4	2.66	3.14	0.53	28.24%
b-5	2.66	3.18	0.55	30.03%
b-6	2.72	3.14	0.50	24.96%
b-7	2.70	3.14	0.51	26.06%
b-8	2.70	3.16	0.52	26.99%

#### 4.2.3 Discussion on electrical characteristics of PMN-PZT based Tm-pMUT array

The thickness-mode pMUT have characteristics of bulk transducer like high acoustic intensity, high electromechanical coupling factor and characteristics of pMUT like high space efficiency. To identify difference with kerfed type, the kerfless type PMN-PZT based Tm-pMUT array was fabricated. The fabricated PMN-PZT based Tm-pMUT array had 8 annular elements. The thickness of PMN-PZT was 300  $\mu\text{m}$ . The fabricated PMN-PZT based Tm-pMUT array was analyzed by impedance analyzer. The measured average resonance frequency and anti-resonance frequency of kerfed type were 2.66 ( $\pm 0.04$ ) and 3.18 ( $\pm 0.03$ ) MHz. The measured effective electromechanical coupling coefficient ( $k_{\text{eff}}^2$ ) of kerfed type was 30.05%. However, the measured average resonance frequency and anti-resonance frequency of kerfless type were 2.69 ( $\pm 0.03$ ) and 3.15 ( $\pm 0.02$ ) MHz. The measured  $k_{\text{eff}}^2$  of kerfless type was 26.89 %.

The measured values of resonance frequency and anti-resonance frequency were very similar between kerfed type and kerfless type. Because the resonance frequency was dependent on thickness of piezoelectric material. However, kerfed type PMN-PZT based Tm-pMUT array is expected to have less cross-talk [55, 56].

In the future, this device will be analyzed by laser doppler vibrometer (LDV) and acoustic intensity measurement system (AIMS) for measuring the displacement and acoustic intensity of the PMN-PZT based Tm-pMUT array.



## 5. Conclusions

To overcome the limitations of dicing process for bulk piezoelectric transducer, the micro-electro-mechanical-system (MEMS) technologies were adopted. The membrane type pMUT has some advantages over bulk type ultrasonic transducer. Compared to bulk piezoelectric transducer, the space efficiency is high. Also, total system dimension is smaller than bulk transducer. Because of this advantages, pMUT has a potential to replace the bulk piezoelectric transducer in some research areas like cell stimulation, cell manipulation. However, generally the acoustic intensity of membrane type pMUT was weaker than bulk transducer. The electromechanical coupling factor was smaller than bulk transducer. To overcome this problem, this research proposed thickness-mode pMUT. The thickness-mode pMUT have characteristics of bulk transducer like high acoustic intensity, high  $k_{\text{eff}}^2$  and characteristics of pMUT like high space efficiency.

In this thesis, the PMN-PZT single crystal was used to make Tm-pMUT array. The PMN-PZT single crystal had high piezoelectric constant (2000 pC/N) and electromechanical coupling coefficient (0.9). However, the dry etching characteristics of PMN-PZT single crystal for MEMS devices does not reported. So, the dry etching characteristics of PMN-PZT single crystal were investigated using ICP etching system. The  $\text{BCl}_3/\text{Cl}_2/\text{Ar}$  gas mixture was used to make plasma. The investigated ICP process parameters were RF power, chamber pressure, bias power, gas mixing ratio. The RF power was varied from 200 W to 1000 W. chamber pressure, bias power and gas flow rate were controlled from 50 W to 450 W, 20 sccm. The optimized condition was  $\text{BCl}_3/\text{Cl}_2/\text{Ar}= 5/2/3$  (10/4/6 sccm), 800 W RF power, 350 W bias power, 2 mTorr chamber pressure. Those optimized ICP etching condition gave a 107.6 nm/min etch rate and 4.22 etch selectivity ratio. The etched PMN-PZT single crystal had polished surface and vertical structure. XPS study performed on clean surface of the PMN-PZT single crystal after

dry etched. XPS analysis revealed that  $\text{BCl}_3/\text{Cl}_2/\text{Ar}= 5/2/3(10/4/6 \text{ sccm})$  plasma was optimized ICP etching condition.

The optimized ICP condition was used to make PMN-PZT based Tm-pMUT array. The fabricated PMN-PZT based Tm-pMUT array analyzed impedance and phase by using impedance analyzer. The average resonance frequency was  $2.66 (\pm 0.04) \text{ MHz}$  and the average anti-resonance frequency was  $3.18 (\pm 0.03) \text{ MHz}$ . The measured effective electromechanical coupling coefficient ( $k_{\text{eff}}^2$ ) was 30.05%. The resonance frequency is important design factor. Because resonance frequency determine the application of the fabricated piezoelectric transducer. For example, the therapy or stimulation system generally have used 500 kHz to 2 MHz resonance frequency and the diagnosis imaging system have used 1 MHz to 10 MHz resonance frequency. The resonance frequencies of PMN-PZT based Tm-pMUT have potential for ultrasound imaging application.

# REFERENCES

- [1] T. Inaoka, H. Shintaku, T. Nakagawa, S. Kawano, H. Ogita, T. Sakamoto, *et al.*, "Piezoelectric materials mimic the function of the cochlear sensory epithelium," *Proceedings of the National Academy of Sciences*, vol. 108, pp. 18390-18395, 2011.
- [2] A. Abrar, D. Zhang, B. Su, T. Button, K. Kirk, and S. Cochran, "1–3 connectivity piezoelectric ceramic–polymer composite transducers made with viscous polymer processing for high frequency ultrasound," *Ultrasonics*, vol. 42, pp. 479-484, 2004.
- [3] H. Choi, M. Anderson, J. Ding, and A. Bandyopadhyay, "A two-dimensional electromechanical composite plate model for piezoelectric micromachined ultrasonic transducers (pMUTs)," *Journal of Micromechanics and Microengineering*, vol. 20, p. 015013, 2010.
- [4] H. Choi, A. Dalakoti, S. Bose, and A. Bandyopadhyay, "Influence of top electrode design on pMUTs performance," *Sensors and Actuators A: Physical*, vol. 135, pp. 613-619, 2007.
- [5] P. C. Eccardt and K. Niederer, "Micromachined ultrasound transducers with improved coupling factors from a CMOS compatible process," *Ultrasonics*, vol. 38, pp. 774-780, 2000.
- [6] R. Dorey and R. Whatmore, "Electroceramic thick film fabrication for MEMS," *Journal of Electroceramics*, vol. 12, pp. 19-32, 2004.
- [7] R. Whatmore, Q. Zhang, Z. Huang, and R. Dorey, "Ferroelectric thin and thick films for microsystems," *Materials Science in Semiconductor Processing*, vol. 5, pp. 65-76, 2002.
- [8] I. O. Wygant, X. Zhuang, D. T. Yeh, Ö. Oralkan, M. Karaman, and B. T. Khuri-Yakub, "Integration of 2D CMUT arrays with front-end electronics for volumetric ultrasound imaging," *Ultrasonics, Ferroelectrics, and Frequency Control, IEEE Transactions on*, vol. 55, pp. 327-342, 2008.
- [9] Ö. Oralkan, J. Johnson, M. Karaman, U. Demirci, K. Kaviani, T. H. Lee, *et al.*, "Capacitive micromachined ultrasonic transducers: Next-generation arrays for acoustic imaging?," *Ultrasonics, Ferroelectrics, and Frequency Control, IEEE Transactions on*, vol. 49, pp. 1596-1610, 2002.
- [10] H. Choi, J.-L. Ding, A. Bandyopadhyay, and S. Bose, "Finite element analysis of piezoelectric thin film membrane structures," *Ultrasonics, Ferroelectrics, and Frequency Control, IEEE Transactions on*, vol. 54, pp. 2036-2044, 2007.
- [11] H. Choi, J. Ding, A. Bandyopadhyay, M. Anderson, and S. Bose, "Characterization and modeling of a piezoelectric micromachined ultrasonic transducer with a very large length/width aspect ratio," *Journal of micromechanics and microengineering*, vol. 18, p. 025037, 2008.
- [12] R. J. Przybyla, S. E. Shelton, A. Guedes, I. Izyumin, M. H. Kline, D. Horsley, *et al.*, "In-air rangefinding with an aln piezoelectric micromachined ultrasound transducer," *Sensors Journal, IEEE*, vol. 11, pp. 2690-2697, 2011.
- [13] F. Akasheh, T. Myers, J. D. Fraser, S. Bose, and A. Bandyopadhyay, "Development of piezoelectric micromachined ultrasonic transducers," *Sensors and Actuators A: Physical*, vol. 111, pp. 275-287, 2004.
- [14] J. Bamber, "Medical ultrasound: research trends that may drive sensor development," in *Journal of Physics: Conference Series*, 2005, p. 1.
- [15] R. J. Meyer Jr, T. C. Montgomery, and W. J. Hughes, "Tonpilz transducers designed using single crystal piezoelectrics," in *OCEANS'02 MTS/IEEE*, 2002, pp. 2328-2333.

- [16] J. Herbert, "Ceramic Dielectrics and Capacitors, Electrocomponent Science Monographs, Vol. 6," *New York: Gordon and Breach Science Publishers*, 1985.
- [17] A. R. Von Hippel, *Dielectric materials and applications* vol. 2: Artech House on Demand, 1954.
- [18] J. Curie and P. Curie, "Piezoelectric and allied phenomena in Rochelle salt," *Comput Rend Acad Sci Paris*, vol. 91, pp. 294-297, 1880.
- [19] H. Kay, "Preparation and properties of crystals of barium titanate,  $\text{BaTiO}_3$ ," *Acta Crystallographica*, vol. 1, pp. 229-237, 1948.
- [20] G. Shirane and A. Takeda, "Phase transitions in solid solutions of  $\text{PbZrO}_3$  and  $\text{PbTiO}_3$  (I) Small concentrations of  $\text{PbTiO}_3$ ," *Journal of the Physical Society of Japan*, vol. 7, pp. 5-11, 1952.
- [21] J. Kuwata, K. Uchino, and S. Nomura, "Phase transitions in the  $\text{Pb}(\text{Zn}_{1/3}\text{Nb}_{2/3})\text{O}_3$ - $\text{PbTiO}_3$  system," *Ferroelectrics*, vol. 37, pp. 579-582, 1981.
- [22] T. R. Shrout, Z. P. Chang, N. Kim, and S. Markgraf, "Dielectric behavior of single crystals near the  $(1-X)\text{Pb}(\text{Mg}_{1/3}\text{Nb}_{2/3})\text{O}_3$ -(x)  $\text{PbTiO}_3$  morphotropic phase boundary," *Ferroelectrics Letters Section*, vol. 12, pp. 63-69, 1990.
- [23] S. Zhang and F. Li, "High performance ferroelectric relaxor- $\text{PbTiO}_3$  single crystals: Status and perspective," *Journal of Applied Physics*, vol. 111, p. 031301, 2012.
- [24] A. Meitzler, H. Tiersten, A. Warner, D. Berlincourt, G. Couqin, and F. Welsh III, "IEEE standard on piezoelectricity," ed: Society, 1988.
- [25] G. Robert, D. Damjanovic, N. Setter, and A. Turik, "Preisach modeling of piezoelectric nonlinearity in ferroelectric ceramics," *Journal of Applied Physics*, vol. 89, pp. 5067-5074, 2001.
- [26] M. Morozov, "Softening and hardening transitions in ferroelectric  $\text{Pb}(\text{Zr}, \text{Ti})\text{O}_3$  ceramics," 2005.
- [27] D. Damjanovic, "Ferroelectric, dielectric and piezoelectric properties of ferroelectric thin films and ceramics," *Reports on Progress in Physics*, vol. 61, p. 1267, 1998.
- [28] B. Jaffe and W. Cook, "Jr and H. Jaffe, Piezoelectric ceramics," ed: Academic Press, New York, 1971.
- [29] Q. M. Zhang and J. Zhao, "Electromechanical properties of lead zirconate titanate piezoceramics under the influence of mechanical stresses," *Ultrasonics, Ferroelectrics, and Frequency Control, IEEE Transactions on*, vol. 46, pp. 1518-1526, 1999.
- [30] O. Bilgen, M. A. Karami, D. J. Inman, and M. I. Friswell, "The actuation characterization of cantilevered unimorph beams with single crystal piezoelectric materials," *Smart Materials and Structures*, vol. 20, p. 055024, 2011.
- [31] G. T. Hwang, J. Yang, S. H. Yang, H. Y. Lee, M. Lee, D. Y. Park, *et al.*, "A Reconfigurable Rectified Flexible Energy Harvester via Solid-State Single Crystal Grown PMN-PZT," *Advanced Energy Materials*, vol. 5, 2015.
- [32] H. S. Kim, J.-H. Kim, and J. Kim, "A review of piezoelectric energy harvesting based on vibration," *International Journal of precision engineering and manufacturing*, vol. 12, pp. 1129-1141, 2011.
- [33] M.-S. Kim, S.-C. Lee, S.-W. Kim, S.-J. Jeong, I.-S. Kim, and J. Song, "Piezoelectric Energy Harvester for Batteryless Switch Devices," *Japanese Journal of Applied Physics*, vol. 52, p. 10MB25, 2013.
- [34] J.-H. Koh, S.-J. Jeong, M.-S. Ha, and J.-S. Song, "Aging of piezoelectric properties in  $\text{Pb}(\text{MgNb})\text{O}_3$ - $\text{Pb}(\text{ZrTi})\text{O}_3$  multilayer ceramic actuators," *Journal of applied physics*, vol. 96, pp. 544-548, 2004.

- [35] Y. Cao, K. Ha, M. Kim, H. Kang, J.-H. Oh, and J. Kim, "A circular array transducer for photoacoustic imaging by using piezoelectric single crystal lead magnesium niobate–lead zirconate titanate," *Japanese Journal of Applied Physics*, vol. 54, p. 07HD08, 2015.
- [36] K. Ren, Y. Liu, X. Geng, H. F. Hofmann, and Q. M. Zhang, "Single crystal PMN-PT/epoxy 1-3 composite for energy-harvesting application," *Ultrasonics, Ferroelectrics, and Frequency Control, IEEE Transactions on*, vol. 53, pp. 631-638, 2006.
- [37] S. R. Anton, A. Erturk, and D. J. Inman, "Bending strength of piezoelectric ceramics and single crystals for multifunctional load-bearing applications," *Ultrasonics, Ferroelectrics, and Frequency Control, IEEE Transactions on*, vol. 59, pp. 1085-1092, 2012.
- [38] A. T. Cheung, "Dicing advanced materials for microelectronics," in *Advanced Packaging Materials: Processes, Properties and Interfaces, 2005. Proceedings. International Symposium on*, 2005, pp. 149-152.
- [39] S. S. Subasinghe, A. Goyal, and S. A. Tadigadapa, "High aspect ratio plasma etching of bulk lead zirconate titanate," in *MOEMS-MEMS 2006 Micro and Nanofabrication*, 2006, pp. 61090D-61090D-9.
- [40] W. Qiu, Y. Yu, H. R. Chabok, C. Liu, F. K. Tsang, Q. Zhou, *et al.*, "A flexible annular-array imaging platform for micro-ultrasound," *Ultrasonics, Ferroelectrics, and Frequency Control, IEEE Transactions on*, vol. 60, 2013.
- [41] X. Wang, C. J. Ritchie, and Y. Kim, "Elevation direction deconvolution in three-dimensional ultrasound imaging," *Medical Imaging, IEEE Transactions on*, vol. 15, pp. 389-394, 1996.
- [42] K. Snook, C.-H. Hu, T. R. Shrout, and K. K. Shung, "High-frequency ultrasound annular-array imaging. Part I: Array design and fabrication," *Ultrasonics, Ferroelectrics, and Frequency Control, IEEE Transactions on*, vol. 53, pp. 300-308, 2006.
- [43] L. Zhang, X. Xu, C. Hu, L. Sun, J. T. Yen, J. M. Cannata, *et al.*, "A high-frequency, high frame rate duplex ultrasound linear array imaging system for small animal imaging," *Ultrasonics, Ferroelectrics, and Frequency Control, IEEE Transactions on*, vol. 57, pp. 1548-1557, 2010.
- [44] F. S. Foster, J. Mehi, M. Lukacs, D. Hirson, C. White, C. Chaggares, *et al.*, "A new 15–50 MHz array-based micro-ultrasound scanner for preclinical imaging," *Ultrasound in medicine & biology*, vol. 35, pp. 1700-1708, 2009.
- [45] C. Liu, F. Djuth, X. Li, R. Chen, Q. Zhou, and K. K. Shung, "Micromachined high frequency PMN-PT/epoxy 1–3 composite ultrasonic annular array," *Ultrasonics*, vol. 52, pp. 497-502, 2012.
- [46] H. R. Chabok, J. M. Cannata, H. H. Kim, J. Williams, J. Park, and K. K. Shung, "A high-frequency annular-array transducer using an interdigital bonded 1-3 composite," *Ultrasonics, Ferroelectrics, and Frequency Control, IEEE Transactions on*, vol. 58, pp. 206-214, 2011.
- [47] E. J. Gottlieb, J. M. Cannata, C.-H. Hu, and K. K. Shung, "Development of a high-frequency (> 50 MHz) copolymer annular-array, ultrasound transducer," *Ultrasonics, Ferroelectrics, and Frequency Control, IEEE Transactions on*, vol. 53, pp. 1037-1045, 2006.
- [48] C. Shen, S. Long, M. Allerdin, and M. Walton, "Resonant frequency of a circular disc, printed-circuit antenna," *Antennas and Propagation, IEEE Transactions on*, vol. 25, pp. 595-596, 1977.

- [49] J. Jung, S. Kim, W. Lee, and H. Choi, "Fabrication of a two-dimensional piezoelectric micromachined ultrasonic transducer array using a top-crossover-to-bottom structure and metal bridge connections," *Journal of Micromechanics and Microengineering*, vol. 23, p. 125037, 2013.
- [50] H. Lee, "Development of high performance piezoelectric single crystals by using solid-state single crystal growth (SSCG) method," *Handbook of Advanced Dielectric, Piezoelectric and Ferroelectric Materials*, Ed. by Z.-G. Ye, CRC Press, New York, p. 158, 2008.
- [51] S. Zhang, S. M. Lee, D. H. Kim, H. Y. Lee, and T. R. Shrout, "Elastic, Piezoelectric, and Dielectric Properties of 0.71 Pb (Mg<sub>1/3</sub>Nb<sub>2/3</sub>) O<sub>3</sub>–0.29 PbTiO<sub>3</sub> Crystals Obtained by Solid-State Crystal Growth," *Journal of the American Ceramic Society*, vol. 91, pp. 683-686, 2008.
- [52] S. Zhang, S. Lee, D. Kim, H. Lee, and T. R. Shrout, "Temperature dependence of the dielectric, piezoelectric, and elastic constants for Pb (Mg<sub>1/3</sub>Nb<sub>2/3</sub>) O<sub>3</sub>–PbZrO<sub>3</sub>–PbTiO<sub>3</sub> piezocrystals," *Journal of Applied Physics*, vol. 102, p. 114103, 2007.
- [53] S. Zhang, S.-M. Lee, D.-H. Kim, H.-Y. Lee, and T. R. Shrout, "Characterization of Mn-modified Pb (Mg<sub>1/3</sub>Nb<sub>2/3</sub>) O<sub>3</sub>–PbZrO<sub>3</sub>–PbTiO<sub>3</sub> single crystals for high power broad bandwidth transducers," *Applied physics letters*, vol. 93, 2008.
- [54] G. Zhu, R. Yang, S. Wang, and Z. L. Wang, "Flexible high-output nanogenerator based on lateral ZnO nanowire array," *Nano letters*, vol. 10, pp. 3151-3155, 2010.
- [55] C. E. Démoré, J. Brown, and G. R. Lockwood, "Investigation of cross talk in kerfless annular arrays for high-frequency imaging," *Ultrasonics, Ferroelectrics, and Frequency Control, IEEE Transactions on*, vol. 53, pp. 1046-1056, 2006.
- [56] R. Chen, N. E. Cabrera-Munoz, K. H. Lam, H.-s. Hsu, F. Zheng, Q. Zhou, *et al.*, "PMN-PT single-crystal high-frequency kerfless phased array," *Ultrasonics, Ferroelectrics, and Frequency Control, IEEE Transactions on*, vol. 61, pp. 1033-1041, 2014.
- [57] J.-K. Jung and W.-J. Lee, "Dry etching characteristics of Pb (Zr, Ti) O<sub>3</sub> films in CF<sub>4</sub> and Cl<sub>2</sub>/CF<sub>4</sub> inductively coupled plasmas," *Japanese Journal of Applied Physics*, vol. 40, p. 1408, 2001.
- [58] J. Jang, Y. Lee, Y. Lee, J. Lee, and G. Yeom, "Etching characteristics of lead magnesium niobate–lead titanate (PMN–PT) relaxor ferroelectrics," *Surface and Coatings Technology*, vol. 131, pp. 252-256, 2000.
- [59] T.-H. An, J.-Y. Park, G.-Y. Yeom, E.-G. Chang, and C.-I. Kim, "Effects of BCl<sub>3</sub> addition on Ar/Cl<sub>2</sub> gas in inductively coupled plasmas for lead zirconate titanate etching," *Journal of Vacuum Science & Technology A*, vol. 18, pp. 1373-1376, 2000.
- [60] E. Meeks, P. Ho, A. Ting, and R. J. Buss, "Simulations of BCl<sub>3</sub>/Cl<sub>2</sub>/Ar plasmas with comparisons to diagnostic data," *Journal of Vacuum Science & Technology A*, vol. 16, pp. 2227-2239, 1998.
- [61] M. Kim, N.-K. Min, S. J. Yun, H. W. Lee, A. Efremov, and K.-H. Kwon, "On the etching mechanism of ZrO<sub>2</sub> thin films in inductively coupled BCl<sub>3</sub>/Ar plasma," *Microelectronic Engineering*, vol. 85, pp. 348-354, 2008.
- [62] K. Kim, T. O'leary, and N. Winograd, "X-ray photoelectron spectra of lead oxides," *Analytical Chemistry*, vol. 45, pp. 2214-2218, 1973.
- [63] L. Pederson, "Two-dimensional chemical-state plot for lead using XPS," *Journal of Electron Spectroscopy and Related Phenomena*, vol. 28, pp. 203-209, 1982.
- [64] R. Kaufmann, H. Klewe-Nebenius, H. Moers, G. Pfennig, H. Jenett, and H. Ache, "XPS studies of the thermal behaviour of passivated Zircaloy-4 surfaces," *Surface and interface analysis*, vol. 11, pp. 502-509, 1988.

- [65] M.-G. Kang, K.-T. Kim, D.-P. Kim, and C.-I. Kim, "Reduction of dry etching damage to PZT films etched with a Cl-based plasma and the recovery behavior," *Journal of the Korean Physical Society*, vol. 41, pp. 445-450, 2002.
- [66] S. Haukka, E. L. Lakomaa, O. Jylha, J. Vilhunen, and S. Hornitzkyj, "Dispersion and distribution of titanium species bound to silica from titanium tetrachloride," *Langmuir*, vol. 9, pp. 3497-3506, 1993.
- [67] C. Sleight, A. Pijpers, A. Jaspers, B. Coussens, and R. J. Meier, "On the determination of atomic charge via ESCA including application to organometallics," *Journal of electron spectroscopy and related phenomena*, vol. 77, pp. 41-57, 1996.
- [68] P. Steiner and H. Höchst, "X-ray excited photoelectron spectra of LiNbO<sub>3</sub>: A quantitative analysis," *Zeitschrift für Physik B Condensed Matter*, vol. 35, pp. 51-59, 1979.
- [69] S.-B. Kim, Y.-H. Lee, T.-H. Kim, G.-Y. Yeom, and C.-I. Kim, "Etching mechanism of (Ba, Sr) TiO<sub>3</sub> films in high density Cl<sub>2</sub>/BCl<sub>3</sub>/Ar plasma," *Journal of Vacuum Science & Technology A*, vol. 18, pp. 1381-1384, 2000.
- [70] J. K. Lee, T.-Y. Kim, I. Chung, and S. B. Desu, "Characterization and elimination of dry etching damaged layer in Pt/Pb (Zr<sub>0.53</sub>Ti<sub>0.47</sub>) O-3/Pt ferroelectric capacitor," 1999.
- [71] F. F. Duval, R. A. Dorey, R. Wright, Z. Huang, and R. W. Whatmore, "High Frequency PZT Composite Thick Film Resonators," *Integrated Ferroelectrics*, vol. 63, pp. 27-33, 2004.

## 요 약 문

### PMN-PZT 압전 단결정 및 미세가공기술을 이용한 두께진동모드

#### 초음파 트랜스듀서 어레이 제작 및 성능평가

본 연구에서는 PMN-PZT 단결정 및 미세가공기술을 이용한 두께진동모드 초음파 트랜스듀서(Tm-pMUT) 어레이가 제작되었다. 사용된 PMN-PZT 는 고상 단결정 성장법을 이용하여 제조되었다. 왜냐하면 SSCG 공법이 구성성분의 용융없이 불규칙한 구조의 폴리크리스탈 세라믹을 정밀한 압전 세라믹으로 만들 수 있기 때문이다. 그리고 PMN-PZT 기반 초음파 트랜스듀서 어레이는 유도결합 플라즈마(ICP) 식각 기술을 이용하여 제작되었다. 이때,  $\text{BCl}_3/\text{Cl}_2/\text{Ar}$  가스혼합물을 이용하여 PMN-PZT 의 건식식각 특성이 조사되었다. ICP 식각에 사용된 식각 변수는 RF power, 챔버압력, bias power, 가스혼합비이다. PMN-PZT 의 식각률 및 PMN-PZT 와 Ni 의 식각선택비를 RF power 는 200 W ~ 1000 W, bias power 는 50 W ~ 450 W, 가스혼합비는 총 20 sccm 이내에서 변화시키며 조사하였다. 또한, 식각 매커니즘을 규명하기 위해 PMN-PZT 의 표면을 X 선 광전자 분광법(XPS)으로 분석하였다. 그 결과,  $\text{BCl}_3/\text{Cl}_2/\text{Ar}$  가스혼합물로 PMN-PZT 를 ICP 식각하였을때 식각률의 감소 없이 식각 선택비를 증가시키는 효과가 있었고, PMN-PZT ICP 식각에 물리적 식각 효과가 화학적 식각 효과보다 더 우세함을 확인하였다. SEM 이미지를 통해 식각된 PMN-PZT 의 측벽 기울기는 bias power 에 따라 증가한다는 것을 확인했다. 최적 ICP 조건은  $\text{BCl}_3/\text{Cl}_2/\text{Ar}= 5/2/3$  (10/4/6 sccm), 800 W RF power, 350 W bias power, 2 mTorr chamber pressure 였다. 이러한 조건을 통해 107.6 nm/min 의 PMN-PZT 식각률과 4.22 의 Ni 하드 마스크와의 식각선택비를 얻을 수 있었다. PMN-PZT 기반 Tm-pMUT 어레이는 최적화된 ICP 식각조건을 이용하여 제작되었다. PMN-PZT 기반 Tm-pMUT 어레이는 8 개의 원형 요소로 구성되어있다. 사용된 PMN-PZT 단결정의 두께는 300  $\mu\text{m}$  였다. 제작된 트랜스듀서는 임피던스 측정이 되었다. 측정결과 8 개의 요소의 평균 공진주파수는 2.66 ( $\pm 0.04$ ) MHz 였으며, 반공진주파수는 3.18 ( $\pm 0.03$ ) MHz 였다. 이를 통해 측정된 전기기계 결합 계수( $k_{\text{eff}}^2$ )는 계산한 결과 30.05% 였다.



이러한 공진주파수는 기존 연구에서 초음파 영상용으로 사용되는 영역이다. 따라서, PMN-PZT 기반 Tm-pMUT 어레이는 영상용 트랜스듀서로의 가능성을 가지고 있다.

핵심어: Piezoelectric, MEMS, PMN-PZT, Ultrasound, Piezoelectric micromachined ultrasonic transducer (pMUT)